ADVANCED NANOFABRICATION AND SENSING USING INTERFERENCE LITHOGRAPHY

NANOFABRICATION ET DÉTECTION AVANCÉES À L'AIDE DE LA LITHOGRAPHIE D'INTERFÉRENCE

Thesis Submitted to the Division of Graduate Studies
of the Royal Military College of Canada
by

James Leibold
Captain

In Partial Fulfillment of the Requirements for the Degree of
Doctor of Philosophy in Physics

April 2021

Acknowledgements

I would like to thank my supervisor Dr. Ribal Georges Sabat, for his support and encouragement.

I would also like to thank Mr. Peter Snell, for manufacturing the moving mirror fixture.

In addition, I would like to thank Dr. Olivier Lebel, for providing the azo-glass material required for the experiments.

I would like to thank Mr. Austin Diggins for all of the hours he spent creating and testing samples for the moving mirror experiment.

Finally I would like to thank my wife Deirdre and my kids Theodore, Clara, and Evelyn for their constant love and support.

Abstract

This thesis consists of three research papers that have been published in the field of interference lithography and sensing. The first experiment used a modified Lloyd's mirror interferometer to create diffraction gratings with large pitches approaching 24 μm. Gratings with various waveform profiles were observed including saw tooth, Dirac comb, and multiple superimposed sin waves. A theoretical framework was developed in order to predict the pitch of the superimposed gratings by calculating the grazing angle of light from multiple reflections between the mirror and the sample surface. This experiment showed that it is possible to fabricate diffraction gratings in azobenzene functionalized glass that were much larger and with a wider variety of profiles than previously reported. The second experiment used a light interference pattern at around the same pitch as the pixel spacing of a digital camera sensor to create images of a beat interference pattern. The physical length of these beats can be measured using the images and are very sensitive to small changes of angle between the reference laser beam and the Lloyd's mirror interferometer. This angle sensor was shown to have an average accuracy of 3.6 arcsec over a range of 1.47 degrees with a center dead zone of 2 arcmin. The last experiment successfully demonstrates a novel in-line holography technique for creating diffractive optics by using a refractive optical element as the object. In particular Fresnel Zone Plates were created using a small converging object lens and a large plano-convex reference lens. Custom multi-focal lenses were produced by superimposing multiple exposures and focal lines were created by tilting the sample. This demonstrates a flexible, low-cost method of fabricating diffractive optical elements in thin films of azobenzene functionalized glass.

Résumé

Cette thèse se compose de trois articles de recherche qui ont été publiés dans le domaine de la lithographie d'interférence et de la détection. La première expérience a utilisé un interféromètre à miroir de Lloyd modifié pour créer des réseaux de diffraction avec de grands pas approchant 24 μm. Des réseaux avec divers profils de formes d'ondes ont été observés, y compris des dents de scie, un peigne de Dirac et de multiples ondes de sinus superposées. Un cadre théorique a été développé afin de prédire le pas des réseaux superposés en calculant l'angle rasant de la lumière à partir de multiples réflexions entre le miroir et la surface de l'échantillon. Cette expérience a montré qu'il est possible de fabriquer des réseaux de diffraction en verre fonctionnalisé à l'azobenzène qui étaient beaucoup plus grands et avec une plus grande variété de profils que précédemment rapporté. La deuxième expérience a utilisé un motif d'interférence lumineuse à peu près au même pas que l'espacement des pixels d'un capteur d'appareil photo numérique pour créer des images d'un motif d'interférence de battement. La longueur physique de ces battements peut être mesurée à l'aide des images et sont très sensibles aux petits changements d'angle entre le faisceau laser de référence et l'interféromètre à miroir de Lloyd. Ce capteur d'angle s'est avéré avoir une précision moyenne de 3,6 secondes d'arc sur une plage de 1,47 degrés avec une zone morte centrale de 2 arcmin. La dernière expérience démontre avec succès une nouvelle technique d'holographie en ligne pour créer des optiques diffractives en utilisant un élément optique réfractif comme objet. En particulier, les plaques de zone de Fresnel ont été créées en utilisant une petite lentille objet convergente et une grande lentille de référence plan-convexe. Des objectifs multifocaux spécifiques ont été produits en superposant plusieurs expositions et des lignes focales ont été créées en inclinant l'échantillon. Cela démontre une méthode flexible et peu coûteuse de fabrication d'éléments optiques diffractifs dans des films minces de verre fonctionnalisé à l'azobenzène.

Table of Contents

List of Figures

List of Abbreviations

AFM – Atomic Force Microscope

CMOS – Complementary Metal Oxide Semiconductor

DBZ – Double Bounce Zone

DIL – Dynamic Interference Lithography

DLIP – Direct Laser Interference Patterning

DOE – Diffractive Optical Element

DOF – Degrees Of Freedom

DR-1 – Disperse Red 1

EM – Electromagnetic

FWHM – Full Width Half Maximum

FZP – Fresnel Zone Plate

IL – Interference Lithography

LHC – Left Hand Circularly

SBZ – Single Bounce Zone

SPR – Surface Plasmon Resonance

SRG – Surface Relief Grating

TBZ – Triple Bounce Zone

UV – Ultraviolet

CHAPTER 1: INTRODUCTION

1.1 Nanofabrication

As technology has advanced over the past several hundred years, one of the main efforts of scientists and engineers has been the miniaturization of devices. By reducing the size of a piece of technology, it will use less material, be more portable, and will often increase the reliability and efficiency of the device. A historic example is the invention of the pocket watch. Spring wound pocket watches, although mechanically complex, were able to rival and sometimes surpass larger mechanical clocks in accuracy and reliability. English inventor John Harrison was awarded a prize of 10,000 pounds by the British parliament in 1765 for his solution for the longitudinal navigation problem. His invention was a portable sea-watch that proved to be more accurate in the harsh environment of maritime travel than his larger earlier protoypes[1]. Another more recent example of the benefits of miniaturization is the silicon microchip. Billions of solid-state transistors can be manufactured in a single integrated circuit with an area a few centimeters across[2]. The miniaturization of technology has allowed for the mass production of the devices like the smart phone, which benefit from the portability, speed, reliability, and energy efficiency of modern micro-components.

Nanofabrication is the process used to create objects or devices with features measured on the scale of nanometers. Gates et al[3] provides a good overview of the main categories of common nanofabrication techniques. These techniques include photolithography, scanning beam lithography, hard or soft molding or embossing, micro contact printing, scanning probe lithography, edge lithography, and self-assembly methods. Of particular interest to this thesis is the fabrication technique called interference lithography. This method involves using beams of coherent light that, when combined, create a pattern of alternating light and dark bands due to interference. This pattern can be inscribed onto a photoresist or if the laser beams are powerful enough, in some cases can be milled directly on the material in a process called Direct Laser Interference Patterning (DLIP)[4]. Interference lithography is very useful for creating optical elements such as diffraction gratings. Its main advantage is that there is no master mold or photomask required since the pattern comes directly from the geometry of the interfering light. This eliminates a costly and time-consuming step of manufacturing a master pattern, which is required in most of the nanofabrication techniques described above.

The goal of this thesis is to demonstrate advancements in the field of nanofabrication through the use of novel interference lithography techniques and applications.

1.2 Photoinduced movement of azobenzene chromophores

Azobenzene is a compound made of two carbon phenol rings that are attached to nitrogen atoms that share a double bond. These compounds are strong absorbers of light, especially at higher frequencies of the visible spectrum, and so have traditionally been used as red dyes in the textile industry. Azobenzene materials have been long known to exhibit a photo-isomerization effect where the molecule will spontaneously switch to its *cis* isomer from its more stable *trans* configuration when it is exposed to heat or an absorbed frequency of light[5], as seen in Figure 1-1. Furthermore, certain polymer chains containing azobenzene have been seen to exhibit a photomechanical effect that results in the transport of material when illuminated with patterned light. This photomechanical effect may occur at temperatures well under the molecular glass transition temperature of the material[6]. The movement of the molecules is dependent on the polarization of light[7] as well as the gradient of the light intensity[8]. It has been shown that this technique requires a free surface of the azobenzene functionalized material and therefore is not a bulk effect[9]. Azopolymer thin films have also demonstrated a temperature dependence for the photomechanical response where at lower temperatures the illuminated areas undergo photo-expansion and above a certain transition temperature the illuminated areas undergo photo-contraction[10]. There have been many theories developed in order to try and explain the various phenomenon associated with the photomechanical response of azobenzene including: internal pressure causing laminar flow[11], anisotropic diffusion[12], and gradient optical fields[8]. Although the exact method how the photomechanical transport of azobenzene materials occurs is still being debated, the general consensus is that the effect is the result of the photoisomerization process described above. One common application of this discovery is the production of Surface Relief Gratings (SRG) on thin films of these azobenzene functionalized materials when exposed to alternating patterns of light and dark fringes.

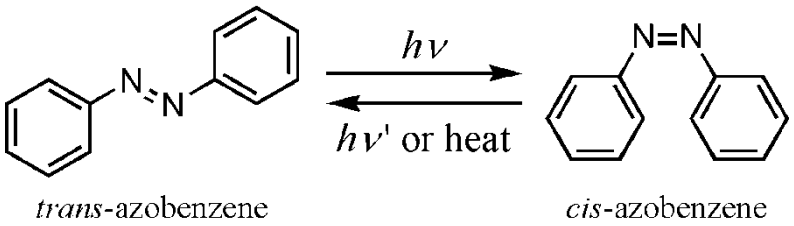

Figure 1-1 – The trans/cis photo-isomerization of azobenzene[a]

The production of SRGs in azobenzene functionalized compounds work very well in conjunction with interference lithography techniques. The photomechanical effect of the azomaterial makes it easy to produce SRGs in this way because the patterned light can be imprinted directly by a simple single-step process without the requirement for developing chemicals or etching. The research group led by Prof. Sabat has been using a molecular glass Disperse Red 1 (DR-1) azobenzene functionalized material to fabricate a wide variety of SRGs in this manner[13]. The main benefits of this novel material are ease of synthesis and higher yields than some other longer molecular azomaterials, such as Poly (methyl methacrylate) azopolymers, also known as PMMA DR-1. The novel molecular glass material is what will be used throughout this thesis and will be referred to as DR-1 azoglass.

There are two main advantages of the fabrication of surface relief patterns using interference lithography on DR-1 azoglass. The first advantage is the speed of the process. A typical measurement for nanofabrication throughput is the produced sample area per unit time and this is measured in units of $\mu m^2 / hr$. High volume production fabrication methods such as UV photolithography have throughputs greater than 10^{12} $\mu m^2 / hr$ [14] while some of the highest resolution nanofabrication techniques such as scanning probe lithography can be as slow as 10^{-5} $\mu m^2 / hr$ [14]. Interference lithography on DR-1 azoglass can produce a 1-cm^2 pattern in minutes and so has a throughput on the order of 10^9 $\mu m^2 / hr$, and this throughput could be increased by using a higher laser power and wider beams. This means that it is very fast and easy to produce samples on a macroscopic scale with feature resolutions on the order of 100 nm. The second main advantage is that interference lithography does not require a photomask or mold. This means that it does not require expensive specialized equipment such

[a] Image from public domain: https://commons.wikimedia.org/wiki/File:Azobenzene_isomerization.png

as the case with scanning beam lithography. Interference lithography techniques should be accessible to any optics lab with a laser in the absorbing band of the material and a few basic optical elements making it a fast and inexpensive way to fabricate customized diffractive optical elements.

1.3 Diffractive optical elements and applications

Diffraction is the phenomenon where a wave travelling in a straight line will change trajectory and spread out when it passes around the edge of an object or through a small hole. Thomas Young's famous double slit experiment in 1803 demonstrates that light does indeed exhibit wave-like properties of diffraction and interference. This discovery paved the way for a theoretical explanation for diffractive optics. Diffractive optical elements such as diffraction gratings use the interference from multiple evenly spaced coherent light sources to modify the path of light. Diffractive optical elements often will have analogous refractive optical elements. For example, a prism can be considered the refractive counterpart of a linear diffraction grating because they both bend and disperse white light in a linear manner. A Fresnel Zone Plate (FZP) can be considered the diffractive counterpart of a traditional refractive lens because they focus light to a focal point. Diffractive optical elements are extremely useful when it comes to miniaturization of optical devices because the patterning of materials can be done at the interface between two thin films. Many devices such as microchips and solar cells already are fabricated using layered construction. The patterning of the interface between these layers to create diffractive elements uses very little material and space, but can have desirable optical properties in miniaturized devices such as lab on a chip[15] or chip based lasers[16]. Diffractive elements such as SRGs also have many useful applications in the field of optics. One of the most common uses for a diffraction grating is as a dispersive element in a spectrometer. Another fairly common application for diffraction gratings is for coupling electromagnetic (EM) energy into optical fibres or waveguides. This technology is therefore extremely useful in the field of communications.

Another area where diffraction gratings are very useful is the field of plasmonics. Diffraction gratings can be used to induce the condition of Surface Plasmon Resonance (SPR) on the surface of conducting materials. An SPR condition can be achieved when the electromagnetic radiation from incoming light couples and resonates with the free electrons in the conducting materials creating a Surface Plasmon Polariton[17]. The resonance conditions for SPR normally requires a wavevector k_{sp} that is slightly larger than the wavevector for a given

frequency of light in the incoming dielectric medium (usually air). Therefore, a prism, diffraction grating, or periodic nanostructures are commonly used to match the momentum and couple the incoming light into the surface of the conductor[18]. The field of plasmonics has many potential applications including enhanced light extraction from LEDs[19], distributed feedback lasers[20], and increasing the efficiency of solar cells[21]. Scientists are also actively working towards the creation of 2D photonic integrated circuits using nanoscale devices such mirrors, beam splitters and waveguides[22]. Another area of particular interest is the plasmonic biosensor. These devices rely on the sensitivity of the SPR on the index of refraction of the dielectric in order to detect small changes at the metal interface[23]. Although the research in this thesis does not specifically investigate SPRs, the creation of nanometer-scaled structures for the manipulation of plasmonic signals is one of the main motivating reasons for advancing interference lithography techniques. The hope is that the knowledge gained by this thesis will act as a steppingstone enabling the production of more advanced plasmonic devices including plasmonic wave guides and biosensors.

1.4 Research Goal and Experiments

The main research goal of this thesis is the advancement of nanofabrication techniques in DR-1 azoglass. Four experiments were conducted with this goal in mind.

The first experiment, described in Chapter 2, tests the upper limit of the pitch of SRGs that can be manufactured on thin films of DR-1 azoglass using interference lithography. Pitches approaching 24 μm were achieved which were much larger than previously published results. The increase in flexibility of producing larger diffraction gratings greatly increases the number of applications of this nanofabrication technique by allowing for diffraction and plasmonic coupling of a broader range of EM radiation beyond visible light and into the infrared region.

The second experiment, in Chapter 3, is a spin-off application that uses the large pitch interference patterns from the first experiment. Its goal is to detect very small changes in angle using an inexpensive complementary metal oxide semiconductor (CMOS) web camera. Thin films of DR-1 azoglass are analogue and continuous and can easily record changes of a few nm to the pitch of the fringes of an interference pattern. Normal off-the-shelf CMOS sensors have pixel sizes on the order of several μm and so do not normally have a good enough resolution to detect small nm scale changes in an interference pattern. However, when one selects the pitch of the interference pattern such that it is close to, but not exactly the same size as the CMOS pixel spacing, this creates a beat pattern that can be imaged by the CMOS sensor.

This interference between the light pattern and the pixel spacing is a form of spatial heterodyning and is somewhat analogous to the interference of the primary and secondary markings on a Vernier scale. This allows for very accurate real-time measurements of the angle of the device by measuring changes to spatial periodicity of the beats in the image.

Another area of interest is the concept of photo-induced mass transport. When a grating is formed in DR-1 azoglass, the molecules are physically moving from one location to another. The work in chapter 2 investigates large pitch gratings in DR-1 azoglass and was able to set some preliminary work in determining how far it is possible to move a molecule using interference lithography in DR-1 azoglass. A dynamic interference lithography (DIL) concept was proposed and tested in a third experiment but did not yield reproducible results. Also, while the research was ongoing, another research group published a similar idea of using a moving mirror to change the phase[24] of an interference lithography experiment. Because the novelty of the research was reduced by this new publication, the thesis work in this area was put on hold. Some preliminary observations are included in the introduction section of this thesis but no journal article was published with these results.

The fourth and final research goal is the production of diffractive optical elements. Because the diffraction gratings in such devices are at similar scales to the wavelength of light being used, advanced nanofabrication techniques are required. Chapter 4 of this thesis details a novel manufacturing technique for diffractive optical elements called inline interference lithography. This method uses ordinary refractive optical elements as objects using inline holography to produce analogous diffractive optical elements. The fact that the holograms are produced co-axially or 'inline' means that fabricated diffractive elements also operate coaxially to the optical axis. These diffractive optical elements may be useful for replacing refractive elements in miniaturized optical devices or as wave concentrators or couplers in photonic devices.

Because of the limited amount of space in the journal articles, the following chapters only provide a basic literature review and explanation of theory. The purpose of the introduction chapter of this thesis is to outline the content and to provide some additional theory and background information for each of the experiments, which was not able to be included in the original articles because of length limitations.

1.5 Large and small scale photo-induced movement for DR-1 Azoglass

Since one of the goals of this thesis is to investigate the limits of nanofabrication on DR-1 azoglass, it seems logical to start with determining the distance scales that it is possible to manipulate the material using interference lithography. A review of literature indicates a common range of grating pitches on azopolymer films from as low as 280 nm[25] to as large as 4600 nm[26] with maximum writing efficiency at around 1000 nm pitch[26]. Grating pitches approaching 200 nm have been reported in azobenzene functionalized thin films with the use of interfering evanescent waves from total internal reflection in a prism[27]. Another paper has demonstrated sub 200 nm grating pitch by using more advanced waveguide mode interference in azopolymers[28]. A third paper reported a pitch of approximately 140 nm being inscribed as a volume grating but not patterned in surface relief[29].

The most obvious way to change the pitch of the gratings being manufactured by IL, besides changing the geometry, is to change the wavelength of the inscribing light. However, a key limitation to interference lithography on an azobenzene functionalized material is that the photo-isomerization process must be induced at an absorbed wavelength of light. For the DR-1 azoglass material, the peak absorbance wavelength is at approximately 485 nm with a full-width-half-maximum of about 175 nm[13]. This range of absorbing wavelengths is one of the main limits to the pitch of the gratings that can be generated using interference lithography.

The article in chapter 2 was able to experimentally demonstrate the fabrication of large pitch SRGs with pitches up to 20 μm using interference lithography. Follow-up research that was done to send samples to another research group for collaborative work resulted in saw tooth gratings with pitches approaching 24 μm as seen at Figure 1-2. However, time constraints did not allow for a full investigation into small pitch gratings. Some initial testing on the use of ultraviolet (UV) patterning on DR-1 azoglass did not yield any useable results and remains an area of active research.

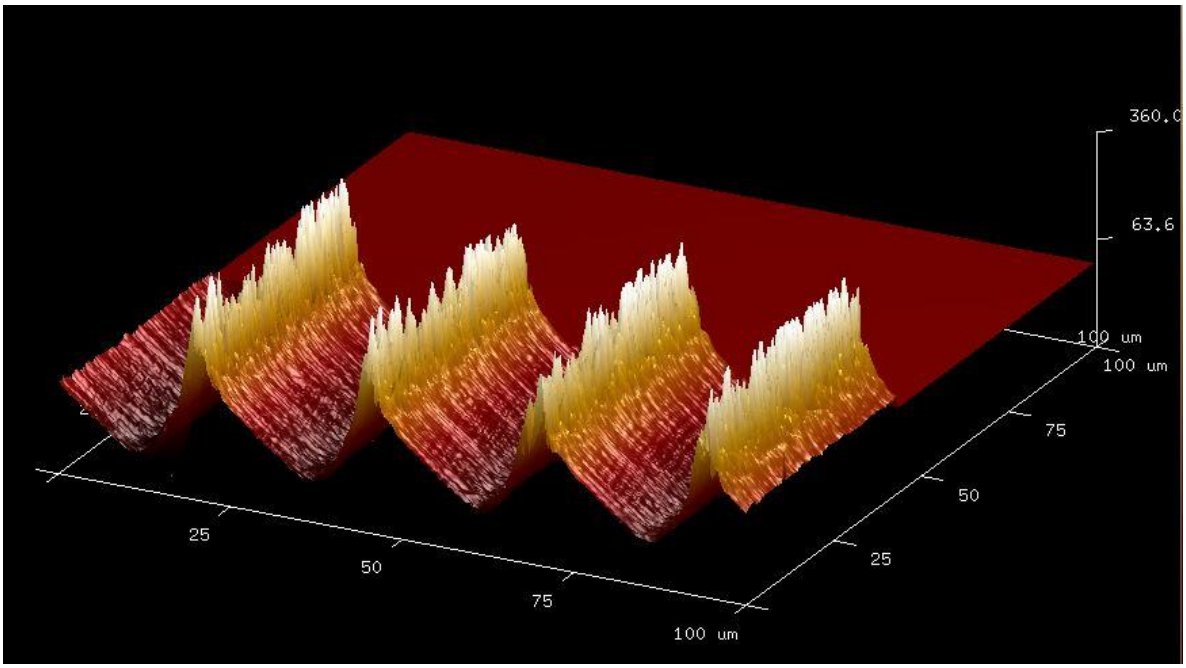

Figure 1-2 – Large scale saw tooth gratins with 24 µm pitch fabricated using interference lithography

1.6 Interference Lithography and the Lloyd's mirror interferometer

One of the first experimental setups that produced SRGs in an azopolymer thin film used a Lloyd's mirror interferometer to create the required interference pattern[26]. In this setup, shown in Figure 1-3, a fixture holds a mirror at a 90-degree angle to the sample thin film. A beam of collimated light is shone half on the mirror and half on the sample where the mirror and sample meet. The result is a sinusoidal interference pattern that is projected onto the sample and is caused by constructive and destructive interference between the directly incident beam and the reflected beam from the mirror.

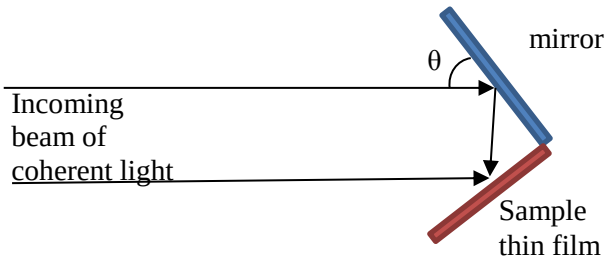

Figure 1-3 – Schematic of a simple Lloyd's Mirror setup for interference lithography

The spacing between maxima of the interference pattern for a Lloyd's mirror is given by[6]

$$\Lambda = \frac{\lambda}{2\sin(\theta)} \tag{1}$$

Where Λ is the grating spacing or 'pitch', λ is the wavelength of interfering monochromatic light, and θ is the angle between the incident light and the mirror.

The main advantage to the Lloyd's mirror setup is that the sample and the mirror are held on the same rigid fixture. Therefore, it is less susceptible to vibrations than a traditional holographic setup with a beam splitter and separate optical elements. The desired pitch of the grating being produced can also be changed very easily by rotating the Lloyd's mirror fixture and changing the angle θ. The geometry of the Lloyd's mirror constrains the range of possible grating pitches. For example, using a range of angles of incident from 5 to 85 degrees with a laser wavelength of 532 nm yields grating pitches between approximately 3 μm and 270 nm.

In order to test the upper limit of grating pitch inscribed in DR-1 azoglass, a modified Lloyd's Mirror setup was used. In this setup, an additional degree of freedom is given to the angle between the mirror and the sample instead of holding it at 90 degrees as is the case with the traditional Lloyd's mirror. Figure 1-5 shows the geometry of the modified Lloyd's mirror where θ is now the angle between the normal of the mirror and the incident light and φ is the angle between the mirror and the sample.

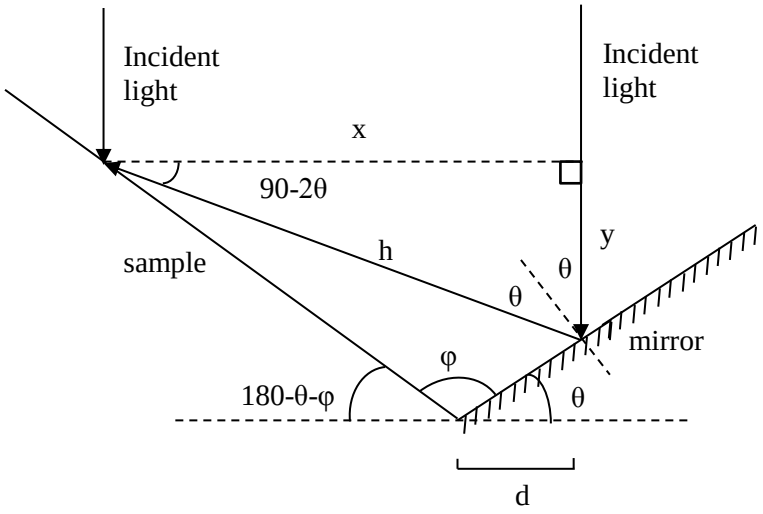

Figure 1-4 – The modified Lloyd's Mirror setup includes variable φ as the angle between the sample and the mirror rather than this angle being fixed at 90 degrees.

A preliminary analysis of the geometry of the setup in Figure 1-4 gives that the pitch Λ of the inscribed grating is given by the equation:

$$\Lambda = \frac{d}{\sin(90^0 + \theta - \varphi)} \tag{2}$$

Here, d is the lateral distance (in the horizontal direction) that the light beam must be moved across the mirror for one interference fringe to be generated on the sample. Given that the path difference δ between the directly incident light striking the sample and the light beam reflected off of the mirror is $\delta = y + h$ and that δ must equal the wavelength of the interfering light λ for one fringe to be created by constructive interference, it can be shown that:

$$d = \frac{\lambda}{\left(1 - \left(\frac{\tan(\theta) + \tan(90^0 - 2\theta)}{\tan(90^0 - 2\theta) - \tan(180^0 - \theta - \varphi)}\right)\right)\left(\tan(90^0 - 2\theta) + \sec(90^0 - 2\theta)\right)} \tag{3}$$

A more elegant approach to determining the pitch of a SRG produced by a modified Lloyd's mirror interferometer is to use the angles of the two incoming beams. Figure 1-5 shows two parallel beams with grazing angle α_1 some distance d apart striking a sample thin film.

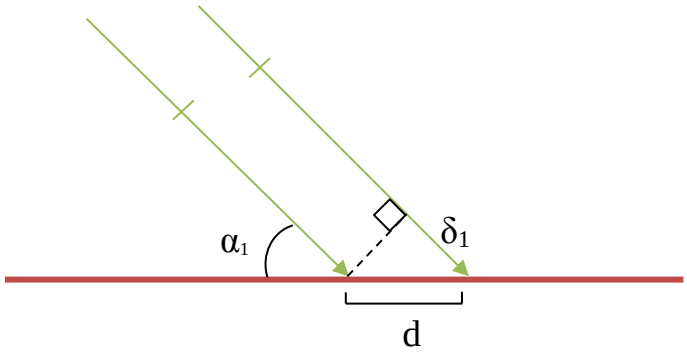

Figure 1-5 – Difference in path length δ between two parallel beams of light with grazing angle α_1

We can show the difference in path length δ between the two beams is given by $\delta_1 = d\cos(\alpha_1)$. If a second pair of parallel beams struck the same two points at a new angle α_2, the path difference between these two beams could likewise be given as $\delta_2 = d\cos(\alpha_2)$. For one full fringe to be projected onto the sample, the path difference between these path lengths must be equal to one wavelength of the inscribing light or $|\delta_1 - \delta_2| = \lambda = |d\cos(\alpha_1) - d\cos(\alpha 2)|$. The distance d on the sample is, under these conditions, equal to the pitch of the interference pattern Λ, and can be isolated to get the equation,

$$\Lambda = \frac{\lambda}{|\cos(\alpha_1) - \cos(\alpha_2)|} \tag{4}$$

In most cases, it is fairly trivial to use ray tracing geometry in order to find the grazing angles α_1 and α_2 of the object and reference beams. This makes a relatively simple way to calculate the pitch of the interference pattern from two beams using equation (4). This equation is used repeatedly in this thesis to determine the predicted pitch in a variety of holographic set-ups.

1.7 Continuously moving interference pattern for inscription on DR-1 azoglass

Writing diffraction gratings on azomaterial films has proven to be a versatile tool in the field of nanofabrication. For example, several articles have demonstrated that multiple gratings can be superimposed on top of each other to form various patterns such as crossed gratings[26] or hex gratings[30]. Although there are numerous examples of multiple separate exposures on azobenzene functionalized thin films, there are very few examples of a continuously changing interference pattern being exposed to a sample film. Several experiments involving the light induced movement of soft bodied robots have used moving light sources or digital micro mirror devices[31]. By adding a moving component to the Lloyd's mirror, it was hypothesized that the sweeping motion of the light interference pattern might enable new grating patterns to be inscribed that were not possible with traditional interference lithography. It was thought that large-pitched gratings might be produced since the surface molecules are continuously swept along by the changing interference pattern. Another possible scenario that was to be tested was the production of gratings with different fill factors or wave forms besides the traditional sinusoidal shape. Lastly, it was hoped that the sweeping motion of the moving interference possible might induce macroscopic large-scale mass transport of the molecules from one side of the sample to the other.

An initial literature search at the time of the thesis proposal revealed that a continuously moving pattern on azo-functionalized films had not been previously studied. Therefore, a piezo-electric actuator was purchased and installed on a custom-built fixture that moved the thin film sample with respect to the mirror. However, as the experiment was underway, new research[24] was published using a piezoelectric controlled mirror to vary the phase of the interference similar to the method proposed in this thesis. Despite being beaten to the mark for the discovery of a new type of interference lithography, a substantial effort was still put into testing of new grating shapes as described above. The two experiments that were attempted are described in the following two sections. Although some preliminary results appeared promising, they were difficult to reproduce and quantify.

The main reasons why the competing research group was able to get superior results with their moving mirror inference lithography experiment was due to two advantages in their experimental set-up. First of all, their experiment inscribes from the reverse side of the azobenzene functionalized film, allowing for in-situ Atomic Force Microscope (AFM) measurements while the grating is being generated. In-situ AFM readings allow for a better

understanding of what speed the moving interference pattern was required to move in order to sweep the azobenzene material and allowed for better control and selection of the experimental variables. Secondly, a closed loop feedback system on the piezo-actuator used to change the position of one of the mirrors allowed for a much greater degree control that the open control system used in the experiment described in this thesis. The moving interference pattern experiment in this thesis was put on hold due to the large amount of time and resources that would have been needed in order to modify the experiment to reach the same capability as the competing research group.

1.8 Moving Mirror Experiment

The experiment shown at Figure 1-6 was created with the goal of testing the effect of a moving interference pattern on the formation of SRGs in DR-1 azoglass thin films. The intent of the moving Lloyd's mirror experiment was to test for the formation of new grating profiles and for photo-induced mass transport of the DR-1 azoglass compound by sweeping a uniform interference pattern over the entire sample.

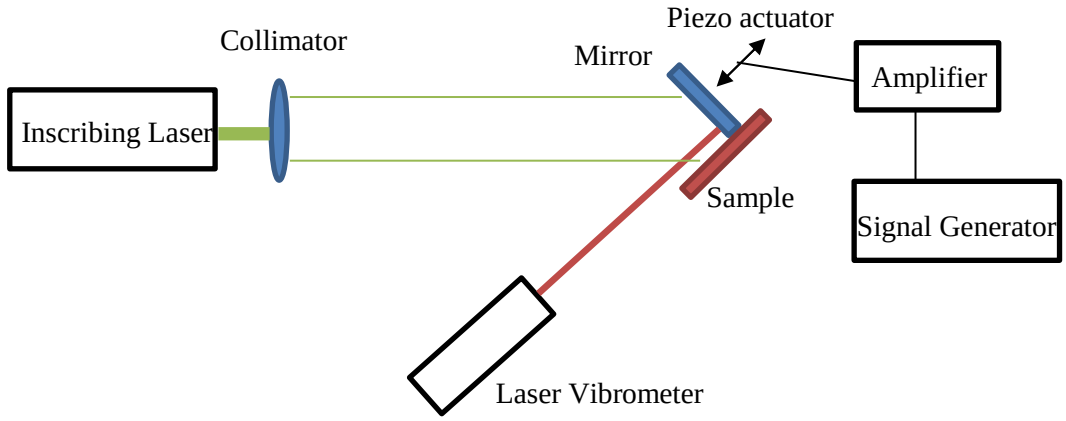

Figure 1-6 - Moving Lloyd's Mirror experiment.

The output voltage of a digital signal generator was amplified to a maximum of 150 V and used to drive a piezoelectric stack with maximum displacement of approximately 10 μm. The piezo-actuator moved a mirror which shifted the phase of the interference pattern on the

sample. The displacement of the mirror was measured using a laser vibrometer. The experimental variables of mirror displacement (amplitude), speed (frequency), and waveform (sine or saw tooth) were controlled by the settings on the signal generator. The angle of the Lloyd's mirror was set to control the pitch of the interference pattern and the laser power controlled the irradiance of the inscribing laser at 532 nm. The length of exposure times for the total inscription process controlled the number of mirror movement cycles occurring in a single exposure. Measurements of the mirror displacement from the vibrometer showed that the piezoelectric actuator suffers from hysteresis, where the same output voltage and frequency on the signal generator do not consistently result in the same displacement of the mirror. A closed-loop feedback system for the mirror displacement would have been able to compensate for this hysteresis resulting in better control of the mirror speed, which is thought to be one of the major factors to control the displacement of the azoglass material using the moving interference pattern. The piezo-actuator appeared to operate most reliably at large displacements, and so signal amplitudes approaching 150 V were most often used. A wide range of frequencies for the signal generator were used to control the speed of the mirror movement, from 0.01 Hz to 10 Hz. A wide range of laser irradiance was tried by controlling the power settings in the range of 0.5 to 3 Watts. Also, a wide range of exposure times from 30 seconds to 20 minutes were investigated. The goal of the experiment was to see if it was possible to find the correct balance of mirror speed and laser irradiance that would result in a 'sweet spot' where the azoglass material would be pushed along by the moving interference pattern. It was hoped that multiple mirror movement cycles with a saw tooth pattern might result in large scale movement of the DR-1 azoglass film due to a repetitive sweeping motion of the light pattern.

Some initial results looked promising where dark coloured bands were observed on the sample under a microscope. These dark bands were scanned using an AFM and seemed to correspond to areas where deeper gratings were being formed. In certain instances, the grating vectors of the SRGs did not correspond to the direction of the light interference pattern and in other cases crossed gratings with two grating vectors, as in Figure 1-8, were produced on the sample. In some instances, the angle of the grating vector of the SRGs seemed to change depending on the experimental parameters such as mirror speed and laser irradiance as seen in Figure 1-7. It was thought that perhaps a 'snowplough' effect was pushing the azoglass at an angle and resulting in different directions of the grating vector. Further testing with similar experimental conditions but with a stationary mirror, revealed that the crossed and angled gratings were likely the result of spontaneous surface gratings[32, 33]. Despite the large number

of trials, over a wide range of variables, no useable correlations were found between gratings pitch, grating vector angle, or depth compared to the speed of the mirror. It is possible that the spontaneous grating formation process dominates grating formation when no static interference pattern is present. Another alternative theory is that the size of the parameter space and the lack of precision in the mirror control system made it too difficult to find the exact parameters where mirror speed was balanced with the inscribing irradiance of the laser in order to move the azoglass material in a predictable way. Future improvements to the experimental set-up could include in-situ AFM scanning and a feedback controlled moving mirror. These modifications already exist in the experimental set-up of a competing research group but might allow for a better control of the variables required to achieve more consistent results.

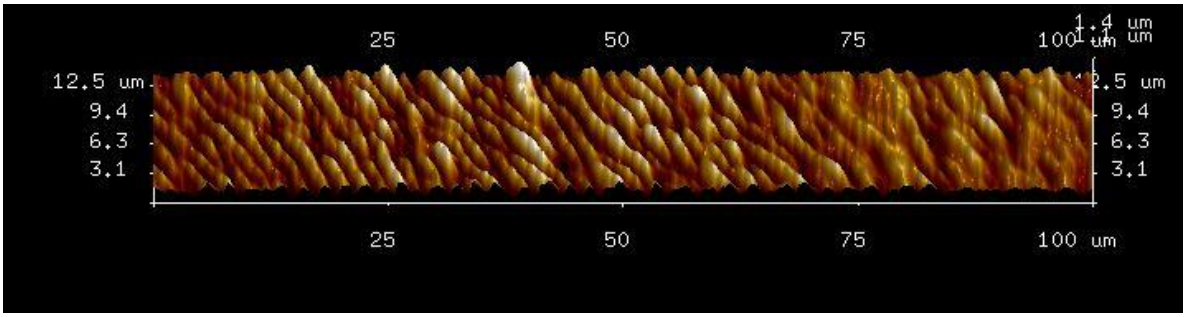

Figure 1-7 – Gratings formed with grating vector approximately 45 degrees from the angle of the vertical inference pattern fringes. This pattern was created by using a moving mirror to sweep the phase of reflected beam while the inscribing laser was illuminating the sample. The results were inconsistent over different areas of the sample and were difficult to reproduce.

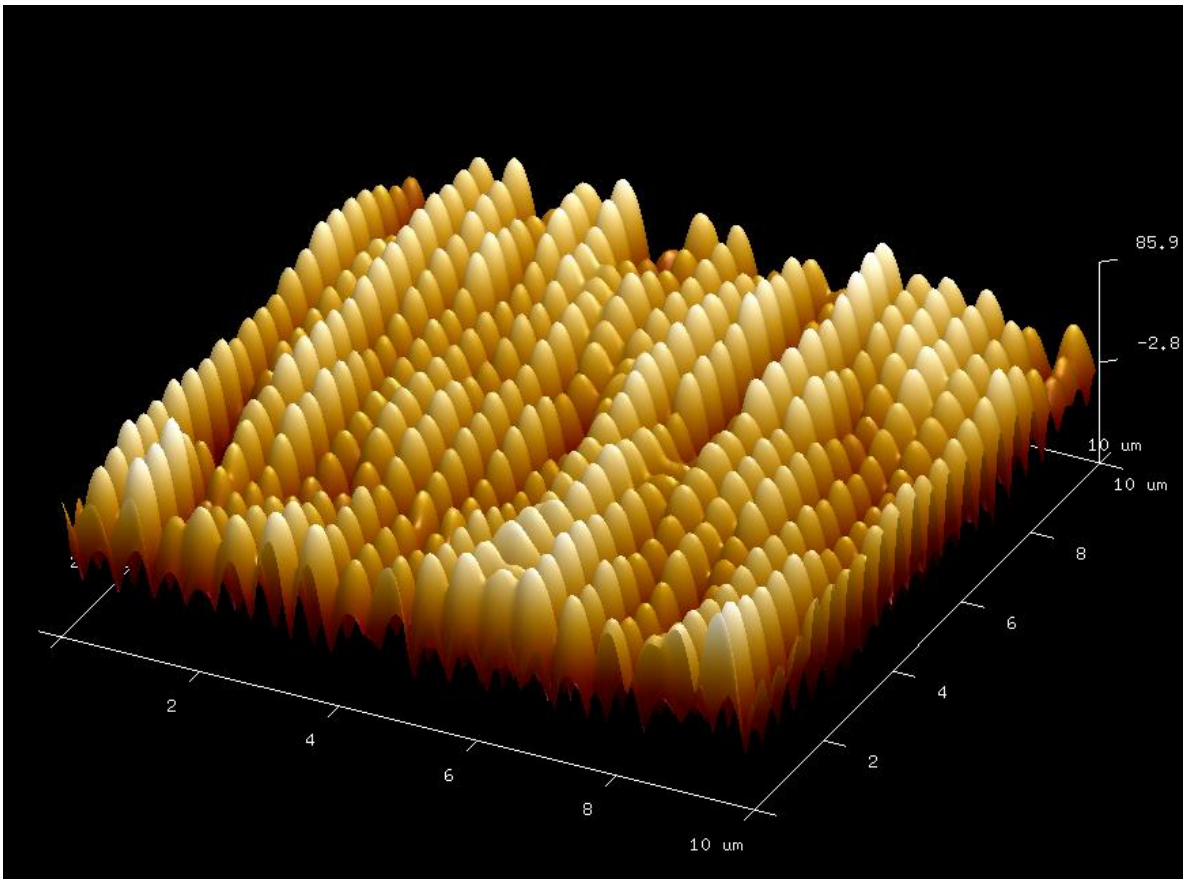

Figure 1-8 – Crossed gratings formed in a single exposure using the moving mirror experiment. Although some very interesting results were observed at different locations on the sample, they were difficult to reproduce and no clear pattern relating mirror speed, laser irradiance and grating pattern was identified. The gratings in the picture could be the result of self-assembling structures or edge effects from the iris that restricted the beam size in the experiment.

1.9 Rotating Lloyd's Mirror Experiment

Because of the difficulties in achieving reliable results in the experiment in the last section, and because of the large parameter space required to find the hypothesized balance point between mirror speed and laser irradiance, a new experiment was devised. A traditional Lloyd's mirror setup shown in Figure 1-3 was used to make a moving interference pattern by slowly rotating the fixture on a staged stepper motor during the inscription process. Similar to the description of the last moving mirror experiment, this rotating mirror creates an interference pattern that will slowly 'sweep' over the sample. Unlike the previous moving mirror experiment, this rotating mirror changes the pitch of the interference of the pattern as it moves instead of keeping a constant pitch with a changing phase. This means that at various points along the sample, the light pattern interference gradient will be changing at different rates due

to the cumulative increase in pitch over many cycles. The result is that the rate of change of the gradient pattern will be different over different areas of the sample as demonstrated in Figure 1-9. This test methodology should, in theory, be helpful for testing a wide range of step increments on a single exposure, because different positions on the same sample represent different speeds that the interference pattern is moving. In practice, it was possible to predict and verify the spacing between 'null' points where the phase shift for each rotation increment was effectively zero because the total shift was some integer multiple of 1 pitch length. For example, if one could imagine that in Figure 1-9 were to continue to a distance of approximately 200 units, there would one such null point near there. The phase of the two waves would be close to alignment after 20 blue waves with a wavelength of 10 units and 19 red waves with a wavelength of 10.5 units These null points formed visible bands of comparatively deep gratings and were the result of the interference pattern being close to static at these null points on the sample as opposed to the moving interference pattern in between the nulls.

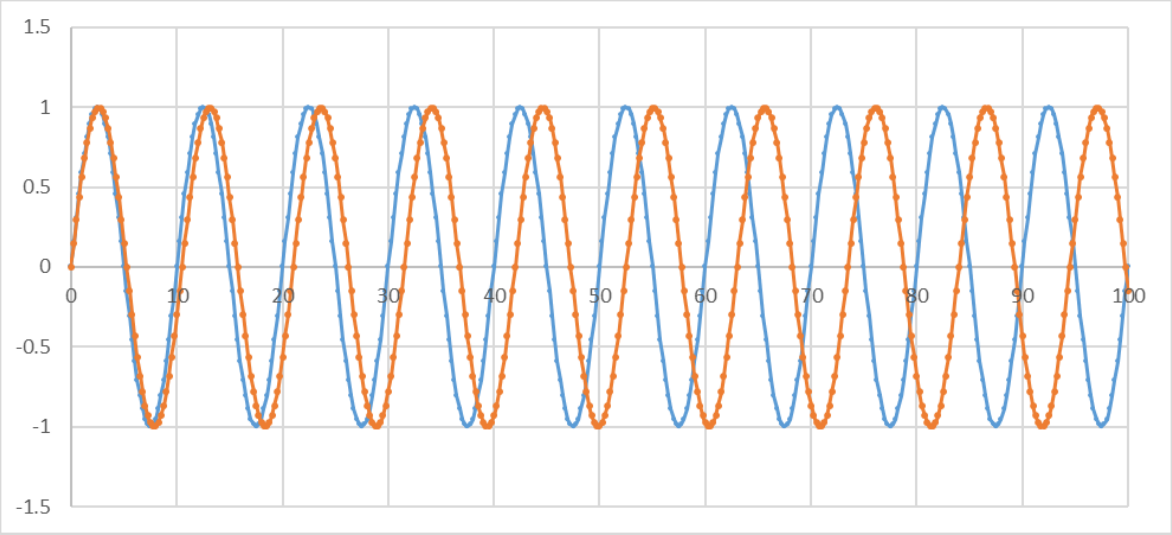

Figure 1-9 – The blue line represents the original pitch of the interference with a wavelength of 10 units, and the orange line represents a 0.5 unit increment in pitch from the rotating Lloyds mirror. It can be seen that the cumulative nature of the 0.5 unit change in pitch results in the phase between the blue and red line varying dependent on the position on the sample.

Some preliminary tests were done, using a 532-nm Verdi laser on a rotating Lloyd's mirror set-up. During an 8000-second exposure starting from a pitch of 350 nm and ending

with a pitch of 400 nm, the mirror was rotated and the grating pitch increased incrementally by 0.25 nm at a time at 10 sec intervals. The results are shown in an AFM image in Figure 1-10

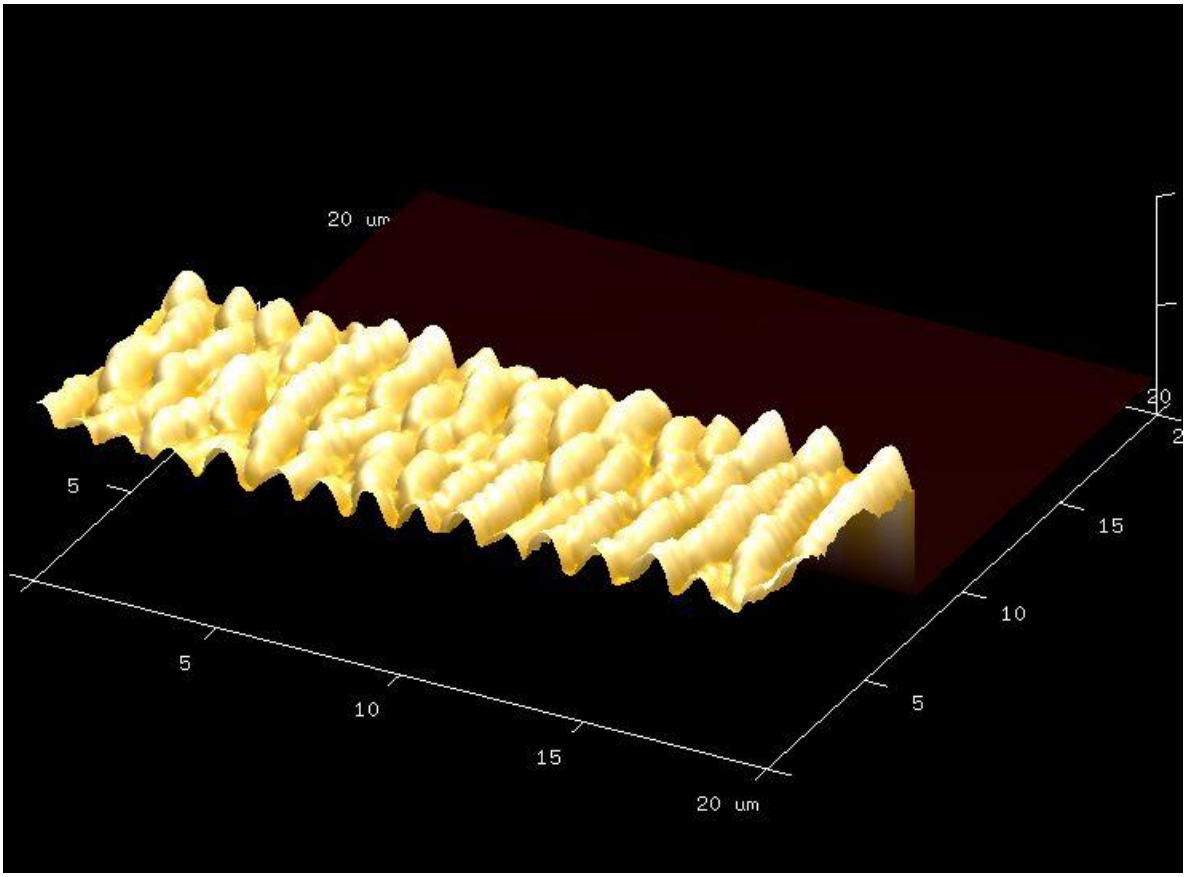

Figure 1-10- AFM imagery of preliminary motion based interference lithography trial. Although the grating is somewhat irregular in form, an average pitch of about 1330 nm was measured. This is much higher than the 350-400 nm pitch range of the interference pattern created by the rotating Lloyd's Mirror

These initial results seemed to indicate that it might be possible to form larger scale features in azo thin films by sweeping the material with a moving interference. However, on closer inspection, these results from the rotating mirror experiment seem to share a close resemblance to results from spontaneous surface grating formation[32]. Control variables for the rotating mirror experiment include, start angle, stop angle, step increment, step time interval, laser power, and total exposure time. Numerous samples were created and tested over a range of parameters. Similar to the moving mirror experiment in the last section, the results of this experiment were difficult to reproduce and were inconclusive. It is postulated that the spontaneous grating formation mechanism dominates in the absence of a stable interference pattern on the sample or that the hypothesized sweeping motion of the material is very sensitive to changes of mirror speed and laser irradiance.

1.10 Inline holography

Inline holography is a type of holographic recording set-up where the reference beam and the interference beam are co-axial. Indeed, some of the earliest holograms were produced by the 'father of holography' Dennis Gabor using co-axial interfering electron beams[34]. This method differs from the more popular off-axis holography where the reference beam hits the holographic recording media at a different angle than the interference beam. The reason that off-axis holograms are most often used is because Gabor's original inline method only works when a small object is placed in the path of a coherent source because of the shadow region shown in Figure 1-11. Another disadvantage to the inline holographic method is that the positive and negative first order diffraction beams cause double images on two different focal planes. This problem was also overcome by off-axis holography because it creates some angular separation between the real and virtual holographic images and allows one image to be viewed at a time.

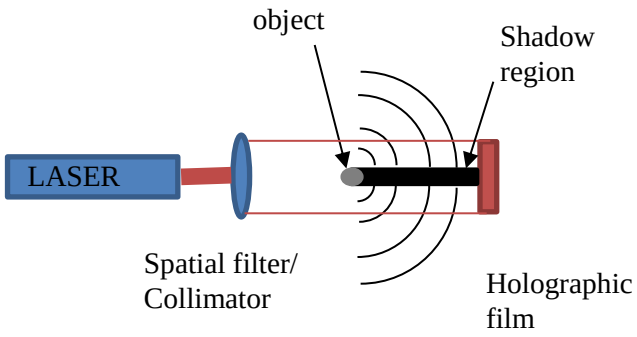

Figure 1-11 – A schematic of Gabor's inline holography method. The object being imaged is necessarily small so that the diffracted light (black arcs) interfere with the directly incident reference beam (area between red lines).

Despite the few disadvantages of inline holography, it is still an active area of research and is used in holographic electron microscopy[35], X-ray holography[36], and inline digital holographic microscopy[37]. There are several advantages to using inline holography. For example, the experimental setup is usually simpler and it does not require a beam splitter. The reason why inline holography is an area of interest for this thesis proposal is not for its imaging applications, but rather because of its potential in the field of nanofabrication.

One of the research goals is the holographic fabrication of diffractive optical elements. In this regard, inline holography offers a major benefit over off-axis holographic techniques. Traditional optical devices such as telescopes or microscopes are designed with co-axial optical elements. If the holographic diffractive optical elements are to behave in a similar fashion as their refractive counterparts, the holographs must be generated in a co-axial or inline method. Holographic images of small lenses have already been inscribed in azoglass using an off-axis Lloyd's Mirror set-up[38] but the resulting focal point is necessarily off-axis[39]. By inscribing the interference patterns of various optical elements directly onto DR-1 azoglass using inline interference lithography, it has been demonstrated that it is possible to fabricate co-axial diffractive optical elements using their refractive counterpart as a template.

1.11 A simple manufacturing method for Fresnel zone plates using inline interference lithography

It is already known that if a small opaque object is placed in the path of a laser beam similar to what is shown in Figure 1-11, the resulting interference pattern will be in the shape of a Fresnel zone plate. The text "Optical Holography" by Collier[34] presents a simple derivation using the geometry in Figure 1-12 .

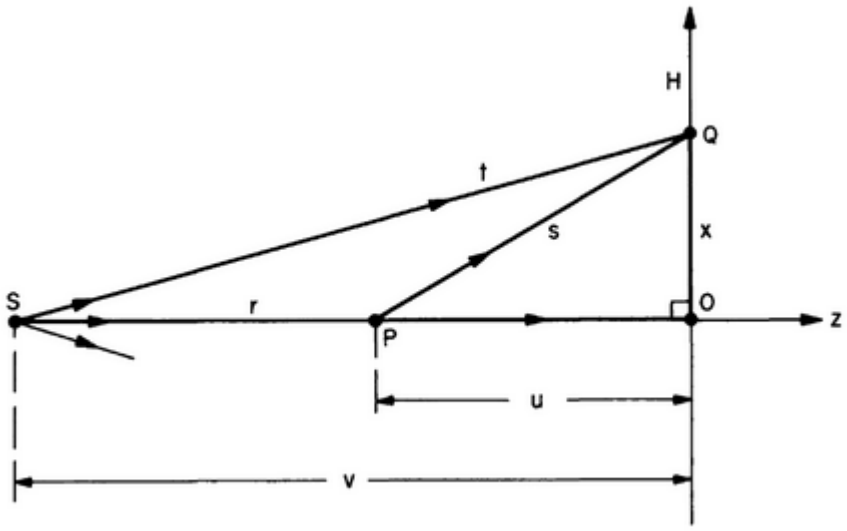

Figure 1-12 – Geometry of a small object P interfering with coherent source of light S to create a Fresnel zone plate using inline holography[34].

The path difference Δl between the source S and the diffracted light from object P is given by the equation:

$$\Delta l = (r+s) - t = (v-u+s) - t$$
$$\Delta l = v - u + (u^2 + x^2)^{1/2} - (v^2 + x^2)^{1/2}$$
$$\Delta l \approx v - u + (u + \frac{x^2}{2u}) - (v + \frac{x^2}{2u}) \quad (1)$$
$$\Delta l \approx \frac{x^2}{2}\left(\frac{1}{u} - \frac{1}{v}\right)$$

This is achieved with use of the paraxial approximation where $u \gg x$ and $v \gg x$.
Using the well know equation for a thin lens:

$$\frac{1}{f} = \frac{1}{u} - \frac{1}{v} \quad (2)$$

where f is the focal length. Substituting this into the result of equation (1) we get:

$$\Delta l \approx \frac{x^2}{2f} \quad (3)$$

Setting the condition for constructive interference for a given path length as $\Delta l = n\lambda$ where n is some integer greater or equal to 0 and λ is the wavelength of the coherent source, we then compare this to equation (3) which yields:

$$\Delta l = n\lambda = \frac{x_n^2}{2f} \quad (4)$$

Here x_n is the radius of the n^{th} bright fringe. This is the same description for the constructive interference condition of a Fresnel zone plate demonstrating that the in-line holograph of a small point generates the geometry of a zone plate with focal length f.

A literature search for holographic zone plates shows that a beam splitting method has been used to manufacture them in azo-doped liquid crystals[40]. Additionally, a zone plate has been fabricated on azopolymer thin films using a zone plate mask[41]. Based on the literature review, it is believed that the implementation of a direct inline interference lithography method for surface relief patterning in thin films of azobenzene functionalized material has not previously been reported.

1.12 Summary

The following 3 chapters are the articles that were published in peer reviewed scientific journals to meet the requirements of this thesis. The article in Chapter 2 is titled “Fabrication of micrometer-scale surface relief gratings in azobenzene molecular glass films using a modified Lloyd's mirror interferometer” and was published in Optical Materials, issue 96 (2019). This paper describes the results from the investigation into the maximum pitch that can be fabricated using interference lithography on DR-1 azoglass films. The article in Chapter 3 is titled “Dual-axis optical spatial heterodyning angle measurements using CMOS sensor color crosstalk” and was published in Sensors and Actuators A, issue 303 (2020). This chapter represents the results from the investigation into whether the interference pattern of a modified Lloyd’s Mirror interferometer could be measured directly using a digital camera sensor. The article in Chapter 4 is titled “Inline holographic inscription of diffractive lenses in azobenzene molecular glass thin films” and was accepted in the journal Applied Optics Vol. 60 No. 10 (2021). This paper investigates a new method of manufacturing diffractive lenses using interference lithography. The results from the moving mirror and rotating mirror experiments described in the introduction were not submitted for publication. Although there are potentially useful applications for the manufacturing of specialized SRG patterns using a moving interference pattern, the lack of predictable results and very large parameter space meant that there was insufficient time to fully investigate the problem.

References

[1] Higgitt, R. F. and Dunn, R., [Finding Longitude: How Ships, Clocks and Stars Helped Solve the Longitude Problem], Collins, Glasgow (2014).

[2] contributors, W. , "Transistor count --- Wikipedia, The Free Encyclopedia," (2018).

[3] Gates, B. D., Xu, Q., Stewart, M., Ryan, D., Willson, C. G. and Whitesides, G. M. , "New Approaches to Nanofabrication: Molding, Printing, and Other Techniques," Chem.Rev. 105(4), 1171-1196 (2005).

[4] Lasagni, A. F., Acevedo, D. F., Barbero, C. A. and Mücklich, F. , "One- Step Production of Organized Surface Architectures on Polymeric Materials by Direct Laser Interference Patterning," Advanced Engineering Materials 9(1- 2), 99-103 (2007).

[5] Rau, H. and Lueddecke, E. , "On the rotation-inversion controversy on photoisomerization of azobenzenes. Experimental proof of inversion," J.Am.Chem.Soc. 104(6), 1616-1620 (1982).

[6] Rochon, P., Batalla, E. and Natansohn, A. , "Optically induced surface gratings on azoaromatic polymer films," Appl.Phys.Lett. 66(2), 136-138 (1995).

[7] Viswanathan, N., Kim, D. and Tripathy, S. , "Surface relief structures on azo polymer films," Journal of Materials Chemistry 9(9), 1941-1955 (1999).

[8] Bian, S., Williams, J. M., Kim, D. Y., Li, L., Balasubramanian, S., Kumar, J. and Tripathy, S. , "Photoinduced surface deformations on azobenzene polymer films," J.Appl.Phys. 86(8), 4498-4508 (1999).

[9] Viswanathan, N. K., Balasubramanian, S., Li, L., Kumar, J. and Tripathy, S. K. , "Surface-initiated mechanism for the formation of relief gratings on azo-polymer films," The Journal of Physical Chemistry B 102(31), 6064-6070 (1998).

[10] Yager, K. G. and Barrett, C. J. , "Photomechanical Surface Patterning in Azo-Polymer Materials," Macromolecules 39(26), 9320-9326 (2006).

[11] Barrett, C. J., Rochon, P. L. and Natansohn, A. L. , "Model of laser-driven mass transport in thin films of dye-functionalized polymers," J.Chem.Phys. 109(4), 1505-1516 (1998).

[12] Lefin, P., Fiorini, C. and Nunzi, J. , "Anisotropy of the photo-induced translation diffusion of azobenzene dyes in polymer matrices," Pure and Applied Optics: Journal of the European Optical Society Part A 7(1), 71 (1998).

[13] Kirby, R., Sabat, R. G., Nunzi, J. and Lebel, O. , "Disperse and disordered: a mexylaminotriazine-substituted azobenzene derivative with superior glass and surface relief grating formation," J.Mater.Chem.C 2(5), 841-847 (2014).

[14] Garcia, R., Knoll, A. W. and Riedo, E. , "Advanced scanning probe lithography," Nature nanotechnology 9(8), 577 (2014).

[15] Duval, D., González-Guerrero, A. B., Dante, S., Osmond, J., Monge, R., Fernández, L. J., Zinoviev, K. E., Domínguez, C. and Lechuga, L. M. , "Nanophotonic lab-on-a-chip platforms including novel bimodal interferometers, microfluidics and grating couplers," Lab on a Chip 12(11), 1987-1994 (2012).

[16] Chen, Y., Li, Z., Zhang, Z., Psaltis, D. and Scherer, A. , "Nanoimprinted circular grating distributed feedback dye laser," Appl.Phys.Lett. 91(5), 051109 (2007).

[17] Maier, S. A., [Plasmonics: Fundamentals and Applications], Springer Science & Business Media (2007).

[18] Barnes, W. L., Dereux, A. and Ebbesen, T. W. , "Surface plasmon subwavelength optics," Nature 424(6950), 824 (2003).

[19] Zhmakin, A. I. , "Enhancement of light extraction from light emitting diodes," Physics Reports 498(4-5), 189-241 (2011).

[20] Chénais, S. and Forget, S. , "Recent advances in solid- state organic lasers," Polym.Int. 61(3), 390-406 (2012).

[21] Mandal, P. and Sharma, S. , "Progress in plasmonic solar cell efficiency improvement: A status review," Renewable and Sustainable Energy Reviews 65, 537-552 (2016).

[22] Ditlbacher, H., Krenn, J. R., Schider, G., Leitner, A. and Aussenegg, F. R. , "Two-dimensional optics with surface plasmon polaritons," Appl.Phys.Lett. 81(10), 1762-1764 (2002).

[23] Hoa, X. D., Kirk, A. and Tabrizian, M. , "Towards integrated and sensitive surface plasmon resonance biosensors: a review of recent progress," Biosensors and Bioelectronics 23(2), 151-160 (2007).

[24] Jelken, J., Brinkjans, M., Henkel, C. and Santer, S., "Rapid optical erasure of surface relief and bulk birefringence gratings in azo-polymer thin films," Photosensitive Materials and their Applications, 1136710 (2020).

[25] Noel, S., Batalla, E. and Rochon, P. , "A simple method for the manufacture of mesoscopic metal wires," J.Mater.Res. 11(4), 865-867 (1996).

[26] Barrett, C. J., Natansohn, A. L. and Rochon, P. L. , "Mechanism of optically inscribed high-efficiency diffraction gratings in azo polymer films," J.Phys.Chem. 100(21), 8836-8842 (1996).

[27] Ohdaira, Y., Hoshiyama, S., Kawakami, T., Shinbo, K., Kato, K. and Kaneko, F. , "Fabrication of surface relief gratings on azo dye thin films utilizing an interference of evanescent waves," Appl.Phys.Lett. 86(5), 051102 (2005).

[28] Wang, X., Zhang, D., Chen, Y., Zhu, L., Yu, W., Wang, P., Yao, P., Ming, H., Wu, W. and Zhang, Q. , "Large area sub-wavelength azo-polymer gratings by waveguide modes interference lithography," Appl.Phys.Lett. 102(3), 031103 (2013).

[29] Ramanujam, P. , "Evanescent polarization holographic recording of sub-200-nm gratings in an azobenzene polyester," Opt.Lett. 28(23), 2375-2377 (2003).

[30] Goldenberg, L. M., Gritsai, Y., Kulikovska, O. and Stumpe, J. , "Three-dimensional planarized diffraction structures based on surface relief gratings in azobenzene materials," Opt.Lett. 33(12), 1309-1311 (2008).

[31] Oscurato, S. L., Salvatore, M., Maddalena, P. and Ambrosio, A. , "From nanoscopic to macroscopic photo-driven motion in azobenzene-containing materials," Nanophotonics 7(8), 1387-1422 (2018).

[32] Ambrosio, A., Girardo, S., Camposeo, A., Pisignano, D. and Maddalena, P. , "Controlling spontaneous surface structuring of azobenzene-containing polymers for large-scale nano-lithography of functional substrates," Appl.Phys.Lett. 102(9), 093102 (2013).

[33] Mazaheri, L., Sabat, R. G., Lebel, O. and Nunzi, J. , "Unraveling the nucleation and growth of spontaneous surface relief gratings," Optical Materials 62, 378-391 (2016).

[34] Collier, R., [Optical Holography], Elsevier (2013).

[35] Latychevskaia, T., Formanek, P., Koch, C. T. and Lubk, A. , "Off-axis and inline electron holography: Experimental comparison," Ultramicroscopy 110(5), 472-482 (2010).

[36] Stockmar, M., Cloetens, P., Zanette, I., Enders, B., Dierolf, M., Pfeiffer, F. and Thibault, P. , "Near-field ptychography: phase retrieval for inline holography using a structured illumination," Scientific reports 3, 1927 (2013).

[37] Sobieranski, A. C., Inci, F., Tekin, H. C., Yuksekkaya, M., Comunello, E., Cobra, D., Von Wangenheim, A. and Demirci, U. , "Portable lensless wide-field microscopy imaging platform based on digital inline holography and multi-frame pixel super-resolution," Light: Science & Applications 4(10), e346 (2015).

[38] Swanson, N. and Sabat, R. G. , "Inscription and analysis of non-uniform diffraction gratings in azobenzene molecular glass thin films," Optics express 26(7), 7876-7887 (2018).

[39] Sabat, R. G. , "Superimposed surface-relief diffraction grating holographic lenses on azo-polymer films," Optics express 21(7), 8711-8723 (2013).

[40] Jashnsaz, H., Nataj, N. H., Mohajerani, E. and Khabbazi, A. , "All-optical switchable holographic Fresnel lens based on azo-dye-doped polymer-dispersed liquid crystals," Appl.Opt. 50(22), 4295-4301 (2011).

[41] Yang, J., Guo, B., Zhang, D., Wang, P. and Ming, H. , "Optically inscribed surface-relief zone plates in azo polymer films," Chinese Optics Letters 5(5), 255-256 (2007).

CHAPTER 2: Fabrication of micrometer-scale surface relief gratings in azobenzene molecular glass films using a modified Lloyd's mirror interferometer

Abstract

Large-scale surface relief diffraction gratings with pitches up to 20 μm were fabricated in thin films of azobenzene molecular glass using a single-step and mask-less photolithography process. A modified Lloyd's mirror interferometer having two degrees of freedom generated an interference pattern that was incident on the azobenzene films. Some of the fabricated gratings had non-periodic profiles resulting from the superposition of multiple sine waves, while others had periodic blazed sawtooth and Dirac comb profiles. Furthermore, careful selection of the experimental parameters resulted in gratings with a beat interference profile having a clearly-visible modulation envelope. A theoretical framework was developed to successfully explain the obtained grating profiles.

2.1 Introduction

Interference Lithography (IL) uses two or more coherent beams of light to create an interference pattern and allows for the fabrication of periodic structures, typically on a sub-micrometer scale, without the need for costly ruling engines, scanning beam systems, or photomasks. Since IL can be considered a form of photolithography, it shares another main advantage in that relatively large areas can be fabricated all at once when the photoresist is exposed to light. This allows for the rapid production of large-scale gratings at a fraction of the cost of other nanofabrication technologies [42]. One common IL method uses a Lloyd's mirror interferometer where one-half of a laser beam is incident on a mirror and the other half is directly incident on a photoresist sample held at 90° with respect to the mirror. When the reflected half-beam from the mirror recombines with the directly incident beam, it generates a sinusoidal interference pattern which is recorded on the photoresist. Several papers in the literature have reported on a modified version of the Lloyd's mirror interferometer where an additional degree of freedom (DOF) is introduced so that the angle between the mirror and the photoresist material is not limited to 90° [43, 44]. These studies demonstrated the ability of the modified Lloyd's mirror interferometer to create lower density (larger pitch) gratings with a better beam coverage than a traditional Lloyd's mirror interferometer. However, to our knowledge, this method of inscribing large-pitch diffraction gratings has never been

accomplished using azobenzene-functionalized materials since they exhibit a completely different grating formation mechanism than more common photoresist materials.

The photomechanical surface patterning of azobenzene-functionalized materials has been the subject of a great deal of research [45]. Of particular interest is their ability to form nanoscale surface relief gratings (SRG) [46, 47] upon exposure to a laser beam interference pattern having a wavelength in the azobenzene film's light absorption spectrum, which is approximately between 430 and 550 nm [48]. The fabrication of SRGs on azobenzene thin films is particularly advantageous because it does not require additional etching, washing, or other processing steps after exposure. There are various published theories that attempt to describe the origin of the photomechanical behavior that allows the inscription of SRGs in azobenzene materials, including: internal pressure causing laminar flow [11], anisotropic diffusion [12], and gradient optical fields [8]. Statistical modelling has proven successful at predicting the motion of azobenzene molecules in a variety of experimental configurations including exposure to laser interference patterns [49]. The common consensus between most published theories is that the photo-induced mass transport of the azobenzene molecule arises from the *trans-cis-trans* photoisomerization of the azobenzene chromophore in the molecules [50]. There are some reports in the literature on the inscription of large-pitch SRGs fabricated in azobenzene-functionalized materials including an 8-μm pitch grating on liquid crystalline azopolymer [51], as well as a 15-μm pitch blazed grating on an azopolymer film [52]. However, in both cases, a photomask was used to produce the required light pattern. Furthermore, gratings with a 10-μm pitch have previously been reported in azopolymer films using a mask-less dual beam IL technique [53]. Another research paper reported on the nanofabrication of blazed gratings by the Fourier reconstruction of a sawtooth and beat interference profiles using multiple laser exposures at different pitches [54]. Surface relief gratings with pitches up to 40 μm have been reported in films of amorphous chalcogenide glasses using polarization modulation from a beam splitting setup [55]. However, the fabrication of chalcogenide films requires thermal deposition and the cured films are then exposed to laser irradiation for over 6 hours to fabricate the gratings. This is contrasted by the fact that azobenzene films are deposited by spin-coating and gratings can be laser-inscribed in only a few minutes.

This paper reports for the first time on the large-scale and mask-less fabrication of SRGs with a pitch greater than 15 μm in azobenzene-functionalized thin films using an IL technique. A Disperse Red 1 (DR-1) azobenzene molecular glass compound [48] was used in combination with a modified two degrees of freedom Lloyd's mirror interferometer to fabricate

micrometer-scale surface relief gratings with a maximum pitch of 20 μm. A simplified theory is presented and successfully used for the prediction of the resulting complicated grating profiles due to the unique laser interference patterns created by the modified Lloyd's mirror interferometer. The large-pitch gratings produced by this method are unique because, for the first time, sawtooth and repeating Dirac function grating profiles are produced in a single-step fabrication process. Also, from the perspective of the photochemistry of the azobenzene material, the gratings reported in this paper are of particular interest since they constitute the first experimental demonstration of azobenzene molecules being transported over relatively long micrometer-scale distances. This is a potential advancement towards the use of azobenzene materials for the creation of novel photo-actuators [56] and for the fabrication of photonic circuits [57], plasmon-enhanced spectroscopes [58] and transmission filters for remote sensing [59] to be used in the infrared regime. Finally, this paper reports for the first time on the fabrication of gratings with a micrometer-scale modulation period or beat envelope.

2.2 Theory

The majority of the double-beam IL experiments found in the literature use a beam splitter and mirrors to direct the two interfering laser beams towards the sample in a symmetrical fashion about a normal to the sample's surface, as illustrated in Figure 2-1 (a). In this case, the pitch Λ of the resulting interference pattern is given by Eq. (1) [42]

$$\Lambda = \frac{\lambda}{2n\sin\left(\frac{\alpha}{2}\right)}, \tag{5}$$

where λ is the wavelength of the inscribing light, n is the index of refraction of the medium above the sample (normally air), and α is the angle between the two beams.

This equation is incompatible with the modified Lloyd's mirror interferometer because the two interfering beams approach the sample at oblique non-symmetrical angles α_1 and α_2, as illustrated in Figure 2-1 (b). An analysis of the optical path difference of this oblique geometry enables the calculation of the pitch of the interference pattern, shown in Eq. (2), where $n \approx 1$:

$$\Lambda = \frac{\lambda}{\left|\cos(\alpha_1) - \cos(\alpha_2)\right|}. \tag{6}$$

As an interesting comparison between Eq. (5) and Eq. (6), the definition of α as the angle between the incoming beams may be used to show that $\alpha_2 = \alpha + \alpha_1$ and this can be substituted into Eq. (6). The result is the simplified Eq. (3), which is similar to Eq. (5) except where the additional factor in the denominator is due to the oblique approach angle of the symmetry of the two beams:

$$\Lambda = \frac{\lambda}{2\sin\left(\frac{\alpha}{2}\right)\sin\left(\alpha_1 + \frac{\alpha}{2}\right)}. \tag{7}$$

This last equation demonstrates that by rotating the sample by an angle of $\alpha_1 + \alpha/2$, so that the approach angle of the two beams is no longer symmetric about the normal, the pitch of the interference pattern can be increased through a projection of the pattern onto the angled sample.

Figure 2-1 (c) illustrates the various angles at which light is incident on and reflected off the sample and the mirror. This figure demonstrates that multiple interference patterns are possible depending on the number of reflections (bounces) back and forth between the sample and the mirror. A geometric analysis based on the angle θ between the mirror and a line perpendicular to the laser beam and the angle φ between the mirror and the sample yields the set of equations used to calculate the approach angles alpha between the different beams and the sample, as presented in Table 2-1.

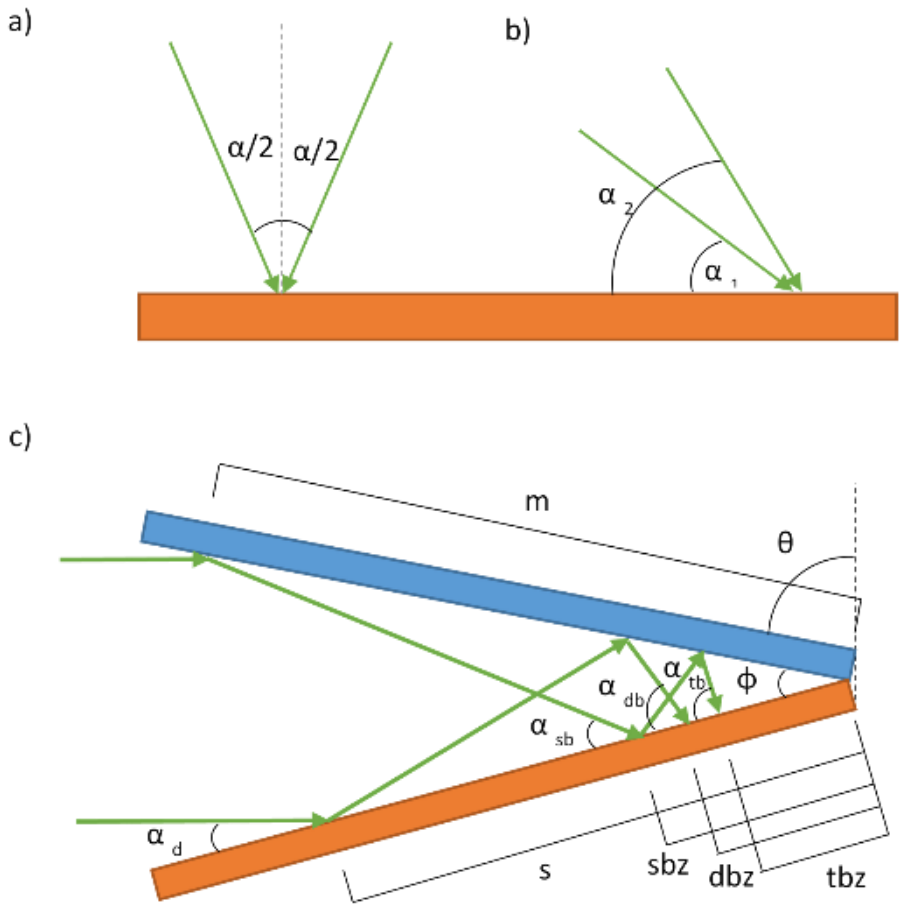

Figure 2-1 - a) Standard double-beam IL where the beams are incident on the sample in a symmetric about the normal. b) A more general case of double-beam IL where the beams are incident on the sample at oblique angles. c) Various angles of light approaching the sample as a result as direct (α_d), single bounce (α_{sb}), double bounce (α_{db}), and triple bounce (α_{tb}) conditions between the sample and mirror. The green arrows represent the beam paths for the outermost extremes of a solid beam of coherent light. m is the distance along the mirror where the solid beam of light ends and s is the distance along the sample where the solid beam of light ends. The single bounce zone (sbz), double bounce zone (d_{bz}), and triple bounce zone (t_{bz}) have been illustrated as areas on the sample where that number of respective bounces are possible. The size and order of these zones may vary depending on specific experimental geometry.

The angles from Table 2-1 are used in conjunction with Eq. (6) to calculate the resulting pitches of various combinations of interfering beams. For example, the dominant grating pitch generally results from the angle of the direct beam α_d interfering with the single bounce beam at an angle of α_{sb}. However, any two angles from Table 2-1 can be combined with Eq. (6) to calculate a corresponding pitch.

Table 2-1. Equations used to calculate approach angles of beams on sample.

Approach condition of beam	Equation based on parameters θ and φ (degrees)
direct (*d*)	$\alpha_d = \theta + \varphi - 90°$
single bounce (*sb*)	$\alpha_{sb} = -\theta + \varphi + 90°$
double bounce (*db*)	$\alpha_{db} = \theta + 3\varphi - 90°$
triple bounce (*tb*)	$\alpha_{tb} = -\theta + 3\varphi + 90°$
quadruple bounce (*qb*)	$\alpha_{qb} = \theta + 5\varphi - 90°$

Figure 2-1 (c) also illustrates that there are certain limited areas or "zones" where the different light beams will interfere with each other. The position of the outermost edges of the laser beam along with the geometry in Figure 2-1 (c) can be used to calculate the outermost edges of the various zones. The size of these zones depends on where the termination of the beam strikes the mirror (*m*), where the termination of the beam on the opposite side strikes the sample (*s*) and the angles of the mirror and the sample (θ, φ). The formulas in Eq. (4) are used to calculate the distance of the edge of each single bounce zone (*sbz*), double bounce zone (*dbz*) and triple bounce zone (*tbz*) zone in relation to the inside edge of the sample closest to the mirror:

$$\begin{aligned} sbz &= m\cos(\theta)\sec(\theta-\phi) \\ dbz &= s\cos(\theta+\phi)\sec(\theta+3\phi) \\ tbz &= m\cos(\theta)\sec(\theta-3\phi). \end{aligned} \tag{8}$$

These equations limit the effective IL exposure area where gratings are formed but they can be modified using the parameters *m* and *s* by changing where the edge of the source beam strikes the fixture using adjustable blinders.

2.3 Experiment

Disperse Red 1 azobenzene molecular glass [48] in powder form was mixed with dichloromethane to obtain a solution of 3% by weight. The solution was shaken and passed through a 0.45-μm filter. Approximately 200 μl of solution was spin-coated on a clean microscope slide at 1000 rpm to form a thin film with a thickness of approximately 600 nm. The azobenzene sample was then placed on the modified Lloyd's mirror interferometer, which was positioned on an optical bench, as depicted in Figure 2-2.

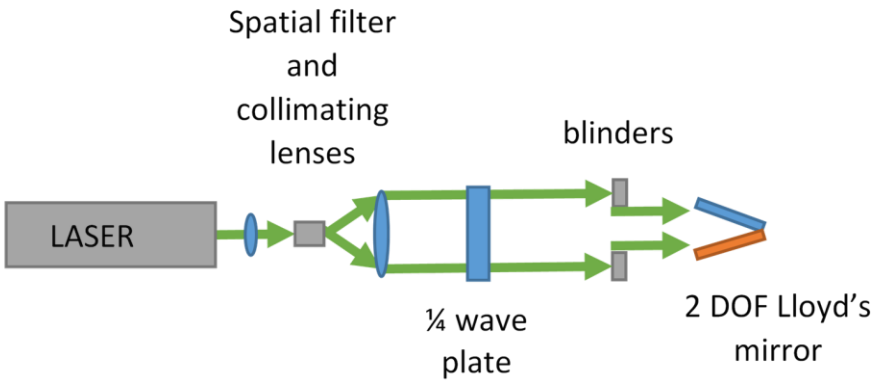

Figure 2-2 - The beam of a Verdi V6 diode pumped laser with a wavelength of 532 nm is passed through a spatial filter and a collimating lens. A quarter-wave plate circularly polarizes the light and a set of blinders controls the position of the edges of the beam. The 2-DOF modified Lloyd's mirror interferometer with independently controlled mirror and sample angles is exposed to the beam with an irradiance of 361 mW/cm^2.

A Coherent Verdi V6 laser with a wavelength of 532 nm was collimated to a beam diameter of approximately 5 cm and used as the inscribing light source. The linearly polarized light from the laser was circularly polarized using a quarter-wave plate. The Lloyd's mirror switches the handedness of the circularly polarized light resulting in interference between left-handed and right-handed circularly polarized light, which is known to be the most efficient polarization configuration for grating creation in azobenzene- functionalized thin films [53]. The angle between the sample and the mirror was initially set to $\varphi = 90°$ and a calibration laser exposure was undertaken to achieve a maximum grating pitch of 2570 nm, as measured using a Bruker Dimension Edge Atomic Force Microscope (AFM). The resulting mirror angle for this grating was calculated to be $\theta = 84.1 \pm 0.1°$ using Eq. (5). This angle θ was held constant for the remainder of the experiment and the angle φ was adjusted using a protractor with an accuracy of $\pm$ 1°. Multiple thin film samples were exposed to the laser beam at angles φ between 7° and 173°. For angles $\varphi < 90°$, the blinders were adjusted with the laser on minimal power so that there was an overlap between the directly incident beam and the single bounce beam. Therefore, there was good separation between the *sbz*, *dbz* and *tbz* zones illustrated in Figure 2-1 (c). For angles $\varphi > 90°$, multiple bounces were not possible, so the blinders were not used in order to maximize the grating surface area. The laser exposure time was initially set to 350 s with a beam irradiance of 361 mW/cm^2, however the exposure time was later increased up to 3600 s for values of $\varphi \geq 170°$. The resulting gratings were imaged and characterized using the AFM. The grating profiles were flattened using a 1st order flattening algorithm and Fourier analysis was performed using the Nanoscope Analysis AFM software.

2.4 Results

At a constant mirror angle of $\theta = 84.1°$, there were limits on the angle φ where the primary grating pitch formed by the interference between beams at angles α_d and α_{sb} could be fabricated. For angles $\varphi < 10°$, the gratings had pitches much smaller than the theory predicted. For instance, a grating inscribed at an angle $\varphi = 7 \pm 1°$ had an average pitch of 7.8 μm instead of the predicted theoretical pitch of 21 μm. It was possible to inscribe gratings at a maximum angle $\varphi = 173°$, but the resulting grating profiles were somewhat noisy over the entire area of laser exposure, as presented in Figure 2-3. As a result, the experimental range of large-scale grating fabrication using this experimental method was determined to be $10° < \varphi < 173°$ with a maximum grating pitch of 20 μm.

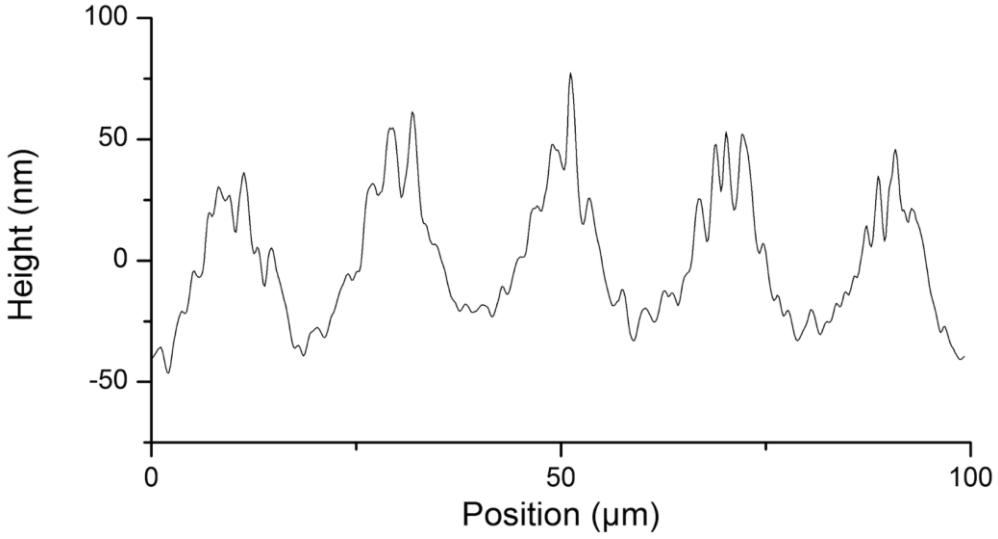

Figure 2-3 - The largest grating pitch produced was approximately 20 μm and resulted from a 3600 s exposure and a sample angle $\varphi = 173 \pm 1°$. The gratings were imperfect due to the fact that they were produced at the limit of this fabrication technique.

For values of $\varphi \geq 170°$, the laser exposure time had to be increased incrementally by a factor of up to 10 times in order to produce gratings that were more than 10 to 20 nm deep. The grating pitch is independent of the laser exposure time but the exposure time is directly related to the grating modulation depth. A plot of the measured grating pitch as a function of angle φ is presented in Figure 2-4 and demonstrates an excellent agreement between the theory and the experiments within the range of possible angles φ.

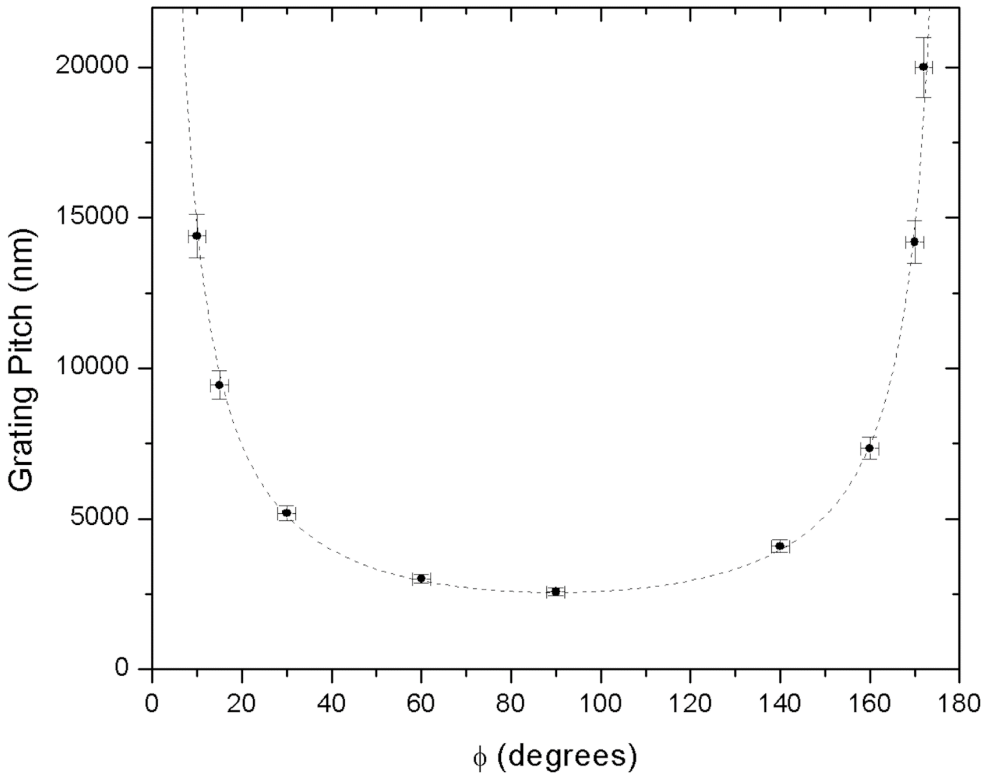

Figure 2-4 - Measured experimental pitches from samples exposed to various angles φ with a constant mirror angle of θ = 84.1 ± 0.1° are marked with black points with error bars. The dashed line represents the theory from Eq. (2) using α_d and α_{sb} from Table 2-1. Note that for angles of φ < 90°, the measured pitches were taken in the single bounce zone so that the effects of multiple bounces could be ignored.

One of the benefits of using angles of φ > 90° is that the fabricated gratings had a uniform pitch without the presence of multi-bounce zones to complicate the pattern. Furthermore, these gratings resulted in interesting non-symmetrical profiles. Examples of such profiles are presented in Figure 2-5 which were inscribed at an angle φ = 170 ± 1°, and with an inscription time of 1400 s. The profile in Figure 2-5 (a) was obtained from the middle of the fabricated grating and it has an average pitch of 14.2 μm with a blazed sawtooth profile. Figure 2-5 (b) shows a sharp grating profile similar to a Dirac comb function. This unique profile was observed at the edge of the same sample closest to the mirror. Figure 2-6 (a) is a 3D AFM image showing a sawtooth grating profile from the same sample presented in Figure 2-5 (b).

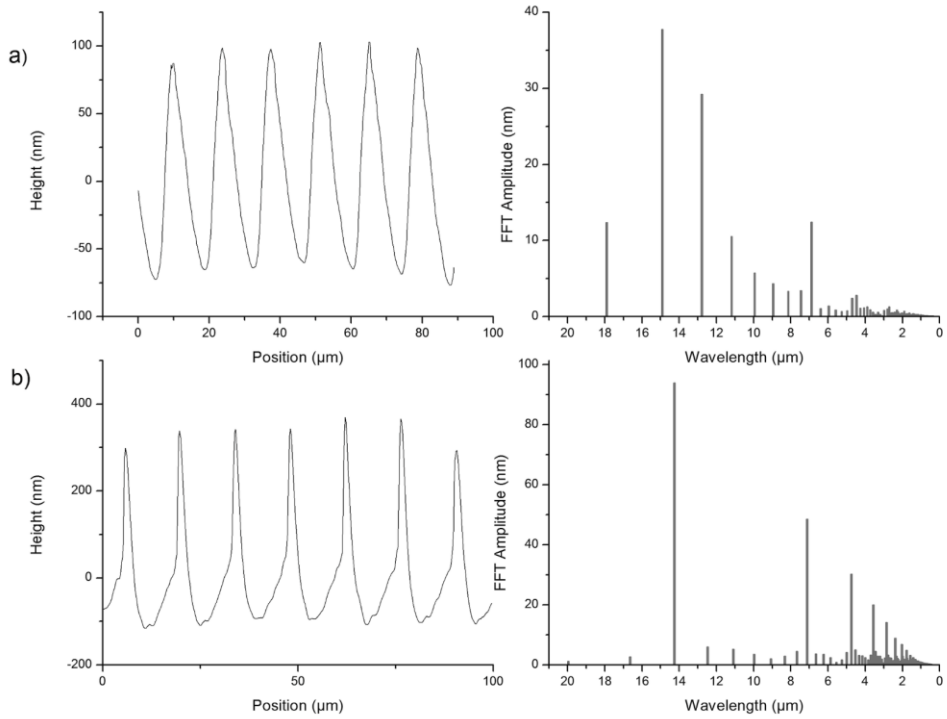

Figure 2-5 - a) A blazed sawtooth grating profile (left) and FFT decomposition of the profile (right) b) A grating profile that resembles a "Dirac comb" (left) and corresponding FFT decomposition (right). The largest Fourier peaks between 14 and 15 μm correspond to the predicted theoretical pitch of 14.9 ± 1.6 μm. Subsequent peaks are thought to be harmonics of the main peak due to the non-sinusoidal shape of the profile.

Gratings fabricated at angles $\varphi < 90°$, with the help of light-blocking blinders, resulted in non-uniform pitches over different areas of the grating due to the different interference zones created by multiple reflections as explained in the theory section. These zones are visible to the naked eye, as pictured in Figure 2-6 (b), and the measured zone sizes correlate well to the theory described by Eq. (4).

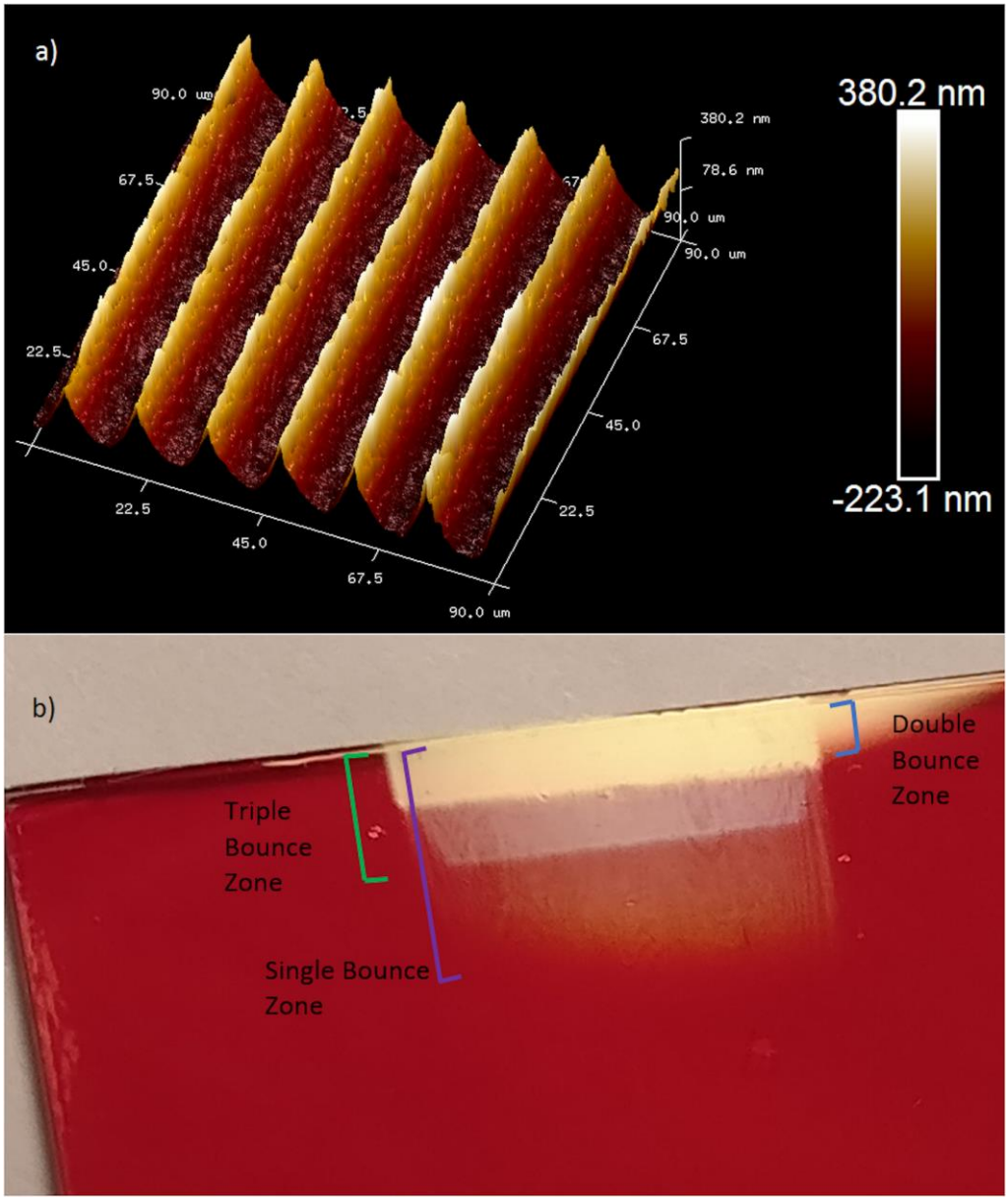

Figure 2-6 - a) Three-dimensional representation of a Dirac comb shaped grating from an AFM scan. b) Photograph of a diffraction grating generated with θ = 84.1 ± 0.1°, φ = 15 ± 1°, *m* = 3.0 ± 0.1 cm and *s* = 9.3 ± 0.1 cm. The different zones corresponding to the number of light bounces between the sample and the mirror are clearly visible and correlate well to the predicted theoretical values of *sbz* = 9.3 cm, *dbz* = 2.2 cm, and *tbz* = 4.3 cm. Contrary to Figure 2-1 (b) the *dbz* zone is smaller than the *tbz* zone due to the specific geometry and blinder position.

In order to further test the theory that multiple reflections are occurring for angles φ < 90°, an AFM scan was taken at the sample edge closest to the mirror on a grating that was fabricated with an angle φ = 10 ± 1° and a single laser exposure of 350 s. The Fourier analysis of the grating profile was then compared to the theoretical pitches calculated using Eq. (6) with

the angles presented in Table 2-1. These results are presented in Figure 2-7. The measured peaks in the Fourier analysis line up very well with the predicted pitches calculated from theory, confirming that the total light pattern on the azobenzene film's surface is caused by the interference of multiple reflections between the sample and the mirror.

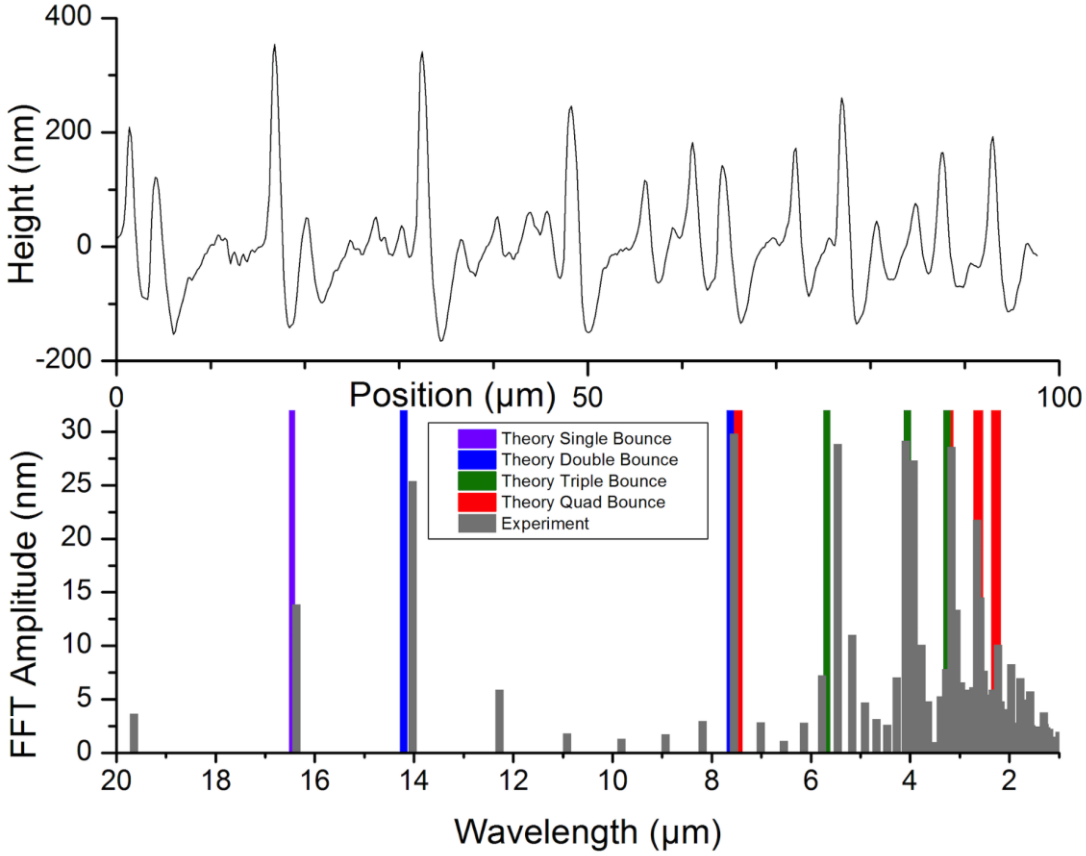

Figure 2-7 - The grating profile (top) shows a complex non-repeating pattern which is the result of the superposition of several sine waves with different periodicities and was fabricated with parameters θ = 84.1 ± 0.1° and φ = 10 ± 1°. The Fourier decomposition of the signal (bottom) agrees with the colored theory bars calculated from angle parameters of θ = 84.2° and φ = 9.2°.

Three AFM scans were taken in the three different interference zones of the same sample shown in Figure 2-6 (b), fabricated with parameters θ = 84.1 ± 0.1° and φ = 15 ± 1°. The Fourier analysis of the profiles were compared to the theory with the results shown in Figure 2-8. The theory once again matches the experimental data very well. The AFM scans from successive zones moving from the inside edge of the grating closest to the interface with the mirror (*dbz*) towards the outside (*sbz*) show a substantial decrease in the Fourier amplitudes of the multi-bounce components until a single-period profile is measured in the single bounce

zone, as predicted by the theory. The experimentally observed Fourier peaks at approximately 3.6 μm and 5.35 μm do not match any theoretical peaks and are thought to be harmonics of the 10.7 μm primary grating pitch. These harmonics are likely the result of the non-sinusoidal grating profiles similar to those observed in Figure 2-5. It is possible that the other peaks caused by the multi-bounce interference zones also have harmonics of their own and may be responsible for some of the noise in the Fourier amplitudes. However, the amplitude of these harmonics is generally low enough so that they can be distinguished from the primary Fourier peaks.

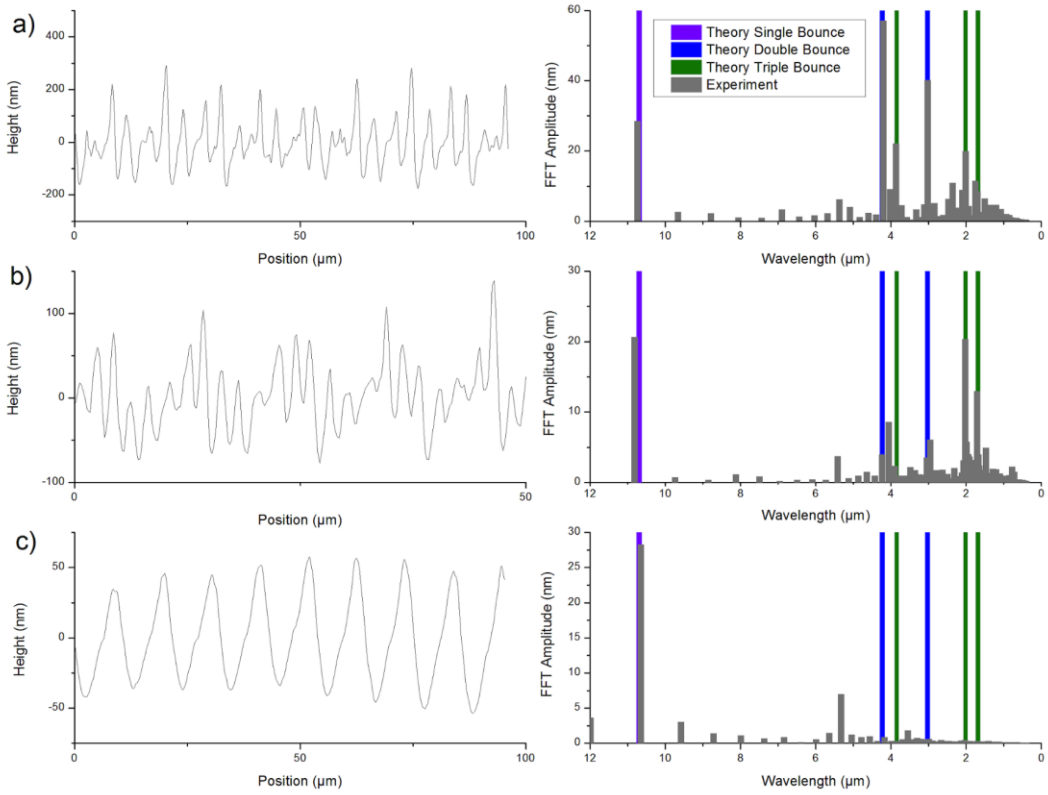

Figure 2-8 - Grating profiles (left) and corresponding Fourier decompositions (right) for a) all zones superimposed, b) only triple bounce and single bounce zones superimposed, and c) only single bounce zone. These zones correspond to the ones shown in Figure 2-6 for a sample fabricated with parameters θ = 84.1 ± 0.1° and φ = 15 ± 1°. The colored bars correspond to the theoretical peaks calculated from θ = 84.0° and φ = 13.8°. The trend of declining grating depths from over 400 nm (for all zones) to approximately 100 nm (for sbz) likely corresponds to the Gaussian profile of the inscribing laser beam. The highest irradiance is at the center of the beam, therefore shallower gratings will be produced away from the center.

It was further hypothesized that if the pitches of two of the interference patterns are closely matched, it is possible to create large-scale wave envelope profiles in a single laser

exposure. The approximate angles $\theta = 70.9°$ and $\varphi = 30°$ were selected based on the theory in order to attempt matching the pitch of the interference pattern from the direct and single reflection beams with the pitch of the pattern from the single and double reflection beams. Figure 2- proves that it is indeed possible to record wave envelope profiles with modulation wavelengths greater than 40 μm in a single laser exposure in azobenzene films, with results well in accordance with the developed theory.

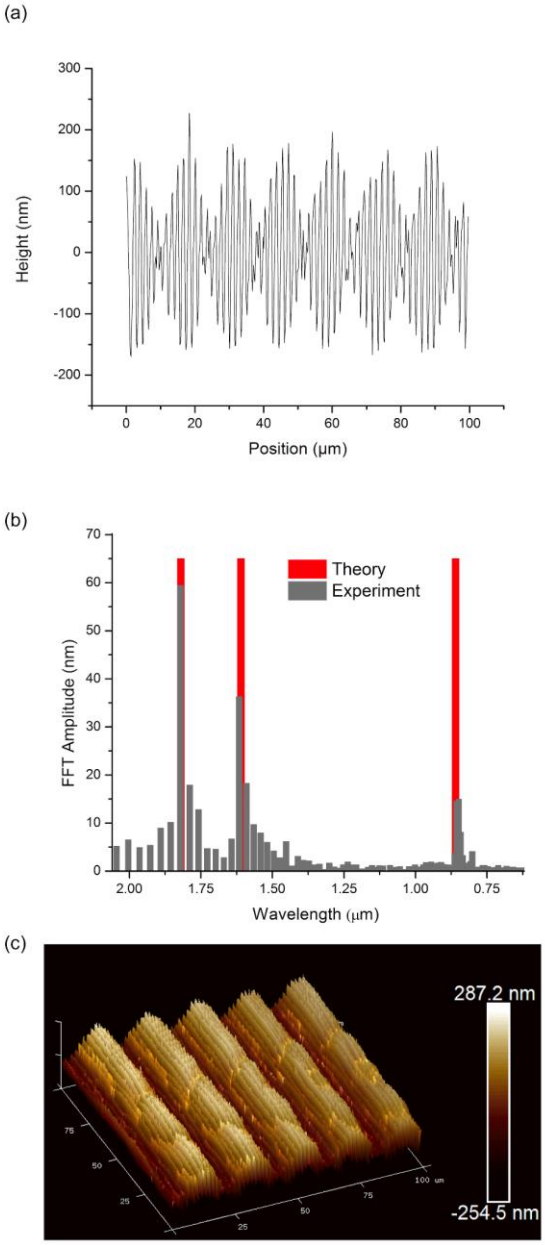

Figure 2-9 - a) Beat interference occurs when two of the interference patterns have close pitch values. b) The FFT analysis of the shown profile indicates pitchs at 1.822 µm from the single reflection, 0.856 µm, from the double reflection and 1.616 µm from the interference between the single and double reflections. The first and last pitches are close enough together that the envelope is clearly seen. The theoretical model was used to match the experimental results in order to calculate the angles of θ = 72.38 ± 0.01° and φ = 28.85 ± 0.01° and predict an envelope period of 28.68 µm. c) A 3D representation of an AFM scan from another sample shows a regular pattern over a 100 µm range with a wave envelope of 40.8 µm with a grating depth approaching 500 nm.

2.5 Discussion

The upper and lower limits of the angle φ from 10° to 173° are of interest because they result in the largest grating pitch that can be produced experimentally using this method. One possible explanation for this limit is that large and small values of φ lead to small angles α_d and α_{sb} which may result in a weakly contrasting interference pattern. If the interference pattern does not have a strong enough contrast between light and dark zones, the azobenzene chromophores do not have enough internal energy gradient for mass transport to occur efficiently. For angles $\varphi < 10°$, it is likely that double or triple bounce interference light beams are overshadowing the very oblique single bounce and direct bounce interference beams resulting in a grating pitch smaller than the theoretically predicted value. For angles $\varphi > 170°$, the weak interference pattern not only requires a longer laser exposure time to produce deep gratings, but it may also contribute to a reduction of the grating quality due to the light beam being more susceptible to noise from imperfections in the mirror and sample surfaces. Surface relief grating depth in azobenzene films is known to be dependent on several parameters including the laser irradiance and polarization, the exposure time, the initial film thickness and the interference pattern contrast [53]. In this experiment, all these parameters were held constant and they resulted in consistent grating depths between 214 nm and 250 nm for a value of φ between 10° and 160°. The notable exceptions are for very large and small angles of φ as previously discussed.

A traditional Lloyd's mirror interferometer would be limited to a maximum grating pitch of approximately 4 μm under normal experimental conditions. A modified Lloyd's mirror is a substantial improvement in that it allows the fabrication of gratings with pitches of up to 20 μm. This method of large-pitch grating fabrication represents a significant increase in flexibility compared to traditional IL fabrication processes on azobenzene-functionalized thin films.

The non-symmetrical grating profiles shown in Figure 2-5 are also noteworthy. It may be possible to explain the asymmetry of the profiles as a direct result of the asymmetry of the incoming beams causing a shadowing effect behind the grating peaks as the grating depth increases. The unusual Dirac comb grating profiles are more difficult to explain. It is clear from the wide troughs and tall peaks that a large amount of azobenzene molecules has been photomechanically displaced. Both the blazed and comb grating profiles came from different locations on the same sample. It is possible that the higher irradiance at the center of the

inscribing Gaussian beam is responsible for the comb profile, while the blazed gratings are generated by a less powerful beam at the outer regions. More detailed experimentation and modeling may be required in order to understand how these unique profile shapes are being generated. It is not known if published azobenzene mass transport theories are capable of explaining the profiles created by extremely large movements of the azobenzene molecules, as seen in the large micrometer-sized gratings produced in this work. However, the production of blazed gratings and Dirac combs in a single exposure IL fabrication method will likely have benefits in other areas of research that require these types of shaped nanostructures.

The theory explaining the multiple beam reflections in the modified Lloyd's mirror interferometer for angles $\varphi < 90°$ is also exciting because it represents a new type of interferometer where one of the reflecting mirrors also doubles as a light sensor. The superposition of multiple sine waves from multiple reflections creates a unique "fingerprint" of patterned light that is inscribed as the grating profile. The Fourier transformation of the profile can be used to analyze this fingerprint and determine the absolute value of θ and φ on a stationary system without the need for counting moving light fringes. This type of interferometer could be used to make sensitive angle measurements for small angles in hard to reach locations. For our research, the parameters θ and φ in the theoretical model were adjusted by increments of up to 0.01° in order to find the theoretical profile that best fit the observed data based on the approximately known start angles. For future work, a computer algorithm that employs statistical methods to determine the parameters of best fit could be used to further increase the accuracy of these measurements. The theory presented in this paper did not include amplitude or phase calculations in its predictions. Although there is some evidence of interference patterns from up to four bounces in Figure 2-7, each successive reflection from the azobenzene film reduces the irradiance of the beam and therefore decreases the interference contrast with the direct beam. For this reason, the theory for a larger number of bounces has been considered negligible. A model that uses the irradiance profile of the beam and the Fresnel reflectance of the azobenzene thin film and mirror might be able to predict the polarization and interference contrast between beams and correlate this to the relative amplitudes of each peak in the Fourier analysis of the resulting gratings. The phase information of the various sine waves in the complex grating profile could also be useful. If the wavelengths of the wave components are not divisible by each other, a non-repeating pattern is generated. The phase information from a particular location of the non-repeating signal inscribed on a sample could be used to calculate accurate length measurements between two points on the grating profile.

The beat interference profiles recorded in the azobenzene molecular glass films are of particular interest because they offer the possibility of fabricating patterns at even larger scales. There is no theoretical limit to the wavelength of the envelope, although extremely sensitive adjustments of the fixture geometry would be required to match the pitches of two patterns in order to produce the largest possible beat periods. This increase in sensitivity from the beats of two interfering patterns could be used in future work to enable for the measurement of angles between the sample and the mirror with extreme accuracy.

2.6 Conclusion

A modified Lloyd's mirror interferometer with an additional degree of freedom for the angle between the sample and mirror was used to produce surface relief gratings with pitches up to 20 μm on thin films of azobenzene molecular glass. A simple mathematical theory was presented and used to successfully predict the grating pitches produced when the sample was positioned at different angles. One unexpected but interesting result is that the large-scale gratings had profile shapes that were not sinusoidal. Some of these profiles closely resembled blazed gratings, while others resembled Dirac combs. Additionally, when the angle between the mirror and the sample was small, multiple reflections occurred and complicated profile patterns of superimposed waves were recorded on the sample. This new type of interferometer generates a unique surface profile pattern that is dependent on the angles of the modified Lloyd's mirror interferometer. The recorded pattern was measured and analyzed using Fourier analysis. The wavelengths of each Fourier component were used along with the presented theory, in order to calculate the two angles of the fixture geometry with resolution of 0.01°. Beat interference envelopes, produced as a special case of this geometry, could theoretically be used to further increase the sensitivity of angle measurements of this type. The results of this experiment were achieved by using a proven single-step fabrication technique that relies on the photomechanical response of azobenzene-functionalized materials. This research has shown that it is possible to fabricate diffraction gratings on azobenzene materials with a much greater range of pitches than previously possible. Also, a more diverse range of grating profiles shapes were produced without the need for multiple exposures. The additional flexibility afforded by this method allows for a greater range of possible applications including the rapid fabrication of diffraction gratings designed for use with infrared light. The gratings produced by this process are extremely cost-effective in terms of equipment and materials and, as a result,

will increase the accessibility of this type of microscale and nanoscale fabrication technology to a wider community.

References

[42] Lu, C. and Lipson, R. , "Interference lithography: a powerful tool for fabricating periodic structures," Laser & Photonics Reviews 4(4), 568-580 (2010).

[43] Wathuthanthri, I., Mao, W. and Choi, C. , "Two degrees-of-freedom Lloyd–mirror interferometer for superior pattern coverage area," Opt.Lett. 36(9), 1593-1595 (2011).

[44] Qian, L., Sheng, B., Huang, Y., Ling, J., Hong, R., Zhang, D., Xu, B., Li, B., Ni, Z. and Zhuang, S. , "Tilted and axis-shift Lloyd's mirror system for recording low-density and large-area holographic grating," Optik-International Journal for Light and Electron Optics 125(3), 1287-1291 (2014).

[45] Priimagi, A. and Shevchenko, A. , "Azopolymer- based micro- and nanopatterning for photonic applications," Journal of Polymer Science Part B: Polymer Physics 52(3), 163-182 (2014).

[46] Rochon, P., Batalla, E. and Natansohn, A. , "Optically induced surface gratings on azoaromatic polymer films," Appl.Phys.Lett. 66(2), 136-138 (1995).

[47] Kim, D., Tripathy, S., Li, L. and Kumar, J. , "Laser- induced holographic surface relief gratings on nonlinear optical polymer films," Appl.Phys.Lett. 66(10), 1166-1168 (1995).

[48] Kirby, R., Sabat, R. G., Nunzi, J. and Lebel, O. , "Disperse and disordered: a mexylaminotriazine-substituted azobenzene derivative with superior glass and surface relief grating formation," Journal of Materials Chemistry C 2(5), 841-847 (2014).

[49] Juan, M. L., Plain, J., Bachelot, R., Royer, P., Gray, S. K. and Wiederrecht, G. P. , "Multiscale model for photoinduced molecular motion in azo polymers," ACS nano 3(6), 1573-1579 (2009).

[50] Lee, S., Kang, H. S. and Park, J. , "Directional photofluidization lithography: micro/nanostructural evolution by photofluidic motions of azobenzene materials," Adv Mater 24(16), 2069-2103 (2012).

[51] Zettsu, N., Ogasawara, T., Arakawa, R., Nagano, S., Ubukata, T. and Seki, T. , "Highly photosensitive surface relief gratings formation in a liquid crystalline azobenzene polymer: new implications for the migration process," Macromolecules 40(13), 4607-4613 (2007).

[52] Minabe, J., Yasuda, S., Kawano, K., Maruyama, T. and Yamada, H. , "Photofabrication of kinoforms as multilevel relief structures on azobenzene-containing polymer films," Japanese journal of applied physics 42(4B), L426 (2003).

[53] Wu, X., Nguyen, T. T. N., Ledoux-Rak, I., Nguyen, C. T. and Lai, N. D. , "Optically Accelerated Formation of One-and Two-Dimensional Holographic Surface Relief Gratings on DR1/PMMA," (2013).

[54] Viswanathan, N., Kim, D. and Tripathy, S. , "Surface relief structures on azo polymer films," Journal of Materials Chemistry 9(9), 1941-1955 (1999).

[55] Asatryan, K., Galstian, T. and Vallee, R. , "Optical polarization driven giant relief modulation in amorphous chalcogenide glasses," Phys.Rev.Lett. 94(8), 087401 (2005).

[56] Mahimwalla, Z., Yager, K. G., Mamiya, J., Shishido, A., Priimagi, A. and Barrett, C. J. , "Azobenzene photomechanics: prospects and potential applications," Polymer Bulletin 69(8), 967-1006 (2012).

[57] Alonso-Ramos, C., Nedeljkovic, M., Benedikovic, D., Penadés, J. S., Littlejohns, C. G., Khokhar, A. Z., Pérez-Galacho, D., Vivien, L., Cheben, P. and Mashanovich, G. Z. , "Germanium-on-silicon mid-infrared grating couplers with low-reflectivity inverse taper excitation," Opt.Lett. 41(18), 4324-4327 (2016).

[58] Petefish, J. W. and Hillier, A. C. , "Multipitched diffraction gratings for surface plasmon resonance-enhanced infrared reflection absorption spectroscopy," Anal.Chem. 87(21), 10862-10870 (2015).

[59] Scherr, M., Barrow, M. and Phillips, J. , "Long-wavelength infrared transmission filters via two-step subwavelength dielectric gratings," Opt.Lett. 42(3), 518-521 (2017).

CHAPTER 3: Dual-axis optical spatial heterodyning angle measurements using CMOS sensor color crosstalk

Abstract

A simple, yet precise, optical angle measurement device was developed by analyzing the light interference pattern from a modified Lloyd's mirror interferometer combined with a CMOS camera sensor. The resulting spatially heterodyned signal was very sensitive to small angle changes from an incident low-power laser beam, with an accuracy better than 8.9 arcsec over a range of 1.47 degrees. Measurement dead zones, estimated to have an angular span of ± 0.96 arcmin, occurred in the middle of the device's measurement range at a critical angle where the pitches of the light interference pattern and the CMOS sensor array were equal. Also, a proof-of-concept test successfully demonstrated the use of this device for dual-axis angle measurements using a single CMOS sensor.

3.1 Introduction

Heterodyning was invented by Reginald Fessenden in 1902 [60] and it consists of combining two radio-frequency signals with slightly different frequencies in order to produce a new set of signals in a new frequency range. A common application of this technique is the super-heterodyne radio receiver [61]. Optical heterodyning can also be achieved with the superposition of two coherent light sources with slightly different frequencies. The mixed heterodyne output signal is highly sensitive to small changes in the frequency of the initial light beams, which allows for an increased sensitivity and a higher signal-to-noise ratio than direct optical measurement devices used in applications such as spectroscopy, lidar, radiometry, interferometry, polarimetry, and imaging [62]. A spatial heterodyning technique can be used to measure the change in the interference pattern as a function of distance rather than time. This technique usually involves using an array of photodetectors to measure spatial separation of interference patterns such as in a spatial heterodyne spectrometer [63].

Several types of optical angle measurement devices have previously been reported in the literature, including optical encoders, auto-collimators, interferometers and systems using total internal reflection or even Surface Plasmon Resonance (SPR). Optical encoders have proven to be dependable with angle measurement accuracies better than 1 arcsec [64], but they require relatively large and precise encoder disks to be manufactured and the sensor must be built into a physical interface between two rotating components. Auto-collimator systems can

measure two simultaneous axes and have very good reported accuracies of 0.01 arcsec [65], but the same report states a limited instrument range of only ±200 arcsec. Although some of the most accurate interferometers have claimed sensitivity as low as 0.057 arcsec/fringe [66], these systems tend to be bulky and can only determine relative angle displacement by counting fringes [67]. Another system that uses the phase shift of different light polarizations in a total internal reflection system cites an error of 1.3% over a range of 0.6 degrees [68]. A SPR-based angle measurement system has an accuracy of 0.2 arcsec, but only over small ranges of ± 4 arcsec [69]. Furthermore, many of these systems are large and require external detectors with multiple optical beam paths in order to function properly.

This work reports on the development of a simple and low-cost angle measurement device that uses a single Complementary Metal Oxide Semiconductor (CMOS) web camera sensor and a small mirror. The device takes advantage of spatial optical heterodyning between the interference pattern formed by a modified Lloyd's mirror interferometer and the spacing of the CMOS sensor elements array in order to create a combined light interference beat pattern that is extremely sensitive to changes in the mirror's angle. Previous papers have reported on the successful capture and recording of interference patterns using camera sensors: Srikanth [70] measured split beam interference patterns on digital camera sensors using an optical magnification technique, while Hochberg *et al.* [71] used a method for projecting the interference pattern from a Lloyd's mirror at highly oblique angles onto a camera array in order to test the sensor's performance. To the best of our knowledge, the work presented herein reports for the first time on the optical measurements of angles using spatial optical heterodyning of a light interference pattern with a CMOS camera sensor. The proposed measurement system can be easily retrofitted on the exterior of an object. Furthermore, it is capable of making absolute angle measurements with respect to a reference laser beam of an object in free space, without the requirement for any external sensors. The prototype device is shown here to have an accuracy better than 8.9 arcsec over a range of 1.47° with an estimated dead zone of approximately 1 arcmin on either side of the central critical angle. A proof-of-concept demonstration has also proven the possibility of obtaining dual-axis angle measurements with a single CMOS sensor. Although the proposed device herein is not as accurate as some of the other published angle measurement devices, its small size, light weight and simplicity will certainly make it useful in many applications, including free-space optical communications, particularly for the acquisition, tracking and pointing of satellites in space [72].

3.2 Theory

In order to estimate the red (R), green (G), and blue (B) color values, most single-sensor cameras have a pattern of alternating color filters placed over each sensor pixel. One of the most common pixel color patterns is called the bayer-pattern, which has twice as many green filters as red or blue ones. Although some color information is necessarily lost using this method, there are a wide variety of image processing techniques called de-bayering that can be employed in order to estimate the missing information through interpolation [73].

Color crosstalk can occur on a CMOS camera sensor when the incorrect color is detected at a pixel location. A diagram of a CMOS sensor is shown in **Error! Reference source not found.** and it depicts a single row of pixels with bayer-pattern filters. Typically, photodiodes in a CMOS sensor are evenly spaced with silicon substrate in between them. To improve the light collection efficiency on each photodiode, micro-lenses are often placed over the filters to focus more light onto their corresponding detector. This sensor architecture is designed to operate for almost normally incident light. If light rays are incident at large oblique angles, it is possible for the incorrect color to be detected and displayed as a result of optical spatial crosstalk [74], as illustrated in the right side pixels of Figure 3-1. Very oblique angles and reflections at boundary interfaces inside the sensor may cause the light signal to skip multiple detector locations. Because the pattern is periodic, as long as the number of pixels skipped is consistent over the device, the results will not differ from single pixel crosstalk besides a possible phase shift. Therefore, for the sake of simplicity these effects have been ignored and the theory assumes a crosstalk shift of one pixel.

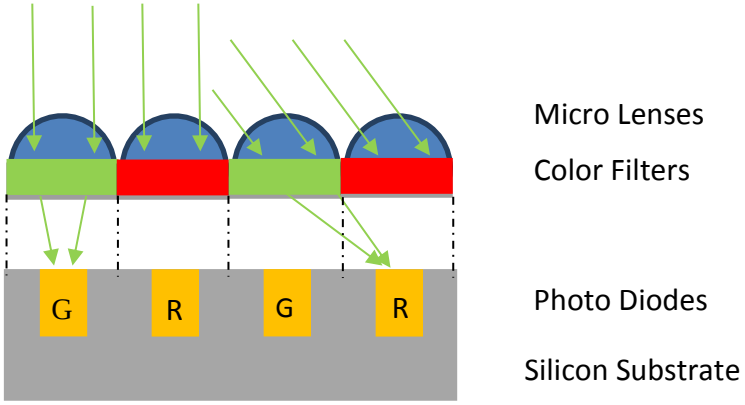

Figure 3-1 - A representative cutaway of a single row of four pixels in a conventional bayer-pattern CMOS sensor.

A traditional Lloyd's mirror interferometer consists of a screen and a mirror placed at right angle. When a coherent beam of light is shone onto the mirror and screen simultaneously, a holographic interference pattern is created on the screen. By changing the angle between the screen and the mirror, it is possible to obtain an interference pattern with a pitch larger than those obtained with a traditional right-angle Lloyd's mirror [43, 44], as depicted in Figure 3-2. The resulting pitch Λ_L of the interference pattern from a modified Lloyd mirror is given by [75]:

$$\Lambda_L = \frac{\lambda}{|cos(\theta + \phi - 90^o) - cos(-\theta + \phi + 90^o)|} \qquad (1)$$

Where λ is the wavelength of the light beam and the angles θ and ϕ are in degrees, as illustrated in Figure 3-2. The angle ϕ between the screen and the mirror in the modified Lloyd's mirror interferometer can be optimized to create an interference pattern with a pitch that is roughly equal to the pitch of the pixel spacing on the CMOS sensor, which replaces the screen in Figure 3-2, in order to create a beat pattern.

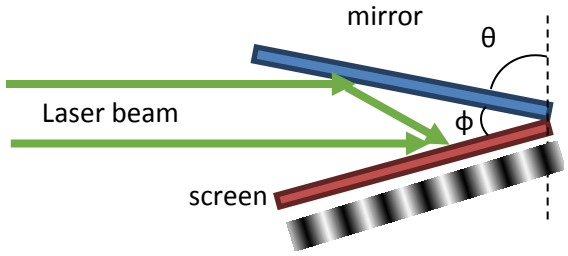

Figure 3-2 - The geometry for a modified Lloyd's mirror interferometer

Considering an interference pattern of amplitude modulated light with a uniform pitch Λ_L projected onto a CMOS sensor with a pixel array pitch Λ_S and knowing that the spatial frequency (f) is inversely proportional to the pitch (Λ), the beat interference equation between two sources $f_{beat} = f_2 - f_1$ can be used to calculate the pitch of the beat periods between the light pattern and the pixel array as follows:

$$\Lambda_{beat} = \frac{1}{\frac{1}{\Lambda_S} - \frac{1}{\Lambda_L}} \qquad (2)$$

As the angle θ is changed by rotating the Lloyd's mirror interferometer, the pitch of the changing light interference pattern (Λ_L) is spatially mixed with the reference pattern from the pixel array spacing (Λ_S) of the CMOS to produce a new heterodyne signal (Λ_{beat}). Combining equation (1) with equation (2) and holding the angle ϕ constant permits the

calculation of the angle θ based on the measured Λ_{beat}. This is the theoretical basis for the proposed angle measurement device in this paper.

3.3 Experiment

A CMOS sensor, having a resolution of 640 by 480 pixels, was removed from a Microsoft lifecam VX-1000 web camera. The width of the active area of the sensor was measured using a travelling microscope with an accuracy of ± 10 μm and divided by 480 to calculate an average pixel spacing of 4.23 ± 0.01 μm. In order to confirm this measurement, a helium-neon laser was shone onto the CMOS sensor and the angles of the first-order diffraction maxima were measured to calculate a pixel array pitch (Λ_S) of 4.20 ± 0.02 μm using the diffraction grating equation. The CMOS sensor was then placed at an angle of $\phi = 40 \pm 1°$ with respect to the Lloyd's mirror and the entire configuration was mounted on a computer-controlled rotary stage with a step size of 0.01°. As seen in Figure 3-3, a laser beam from a Coherent Verdi V6 solid-state laser, emitting at 532 nm wavelength, was expanded and collimated before being incident on the mirror/sensor assembly. Even at the lowest laser power setting of 10 mW, the CMOS sensor was overexposed, so the beam power was further reduced by a 0.43% neutral density filter, resulting in a measured average beam irradiance of 19.8 ± 3.5 mW/m^2. The laser light was S-polarized with respect to the plane of incidence of the mirror but any polarization that produces a well contrasted interference pattern should theoretically work. The resulting light interference pattern from the CMOS sensor was observed on a computer with the "Sharpcap" image capturing software. Although the majority of the laser beam was incident on the mirror and sensor assembly, a small portion of the laser beam was allowed to pass over the CMOS sensor, and it was projected on a screen located 156.5 ± 0.2 cm away. Measurements of the distance, *d*, between the coaxial beam and the reflected beam, were used to calculate a value for the angle θ with an uncertainty of ± 0.02°.

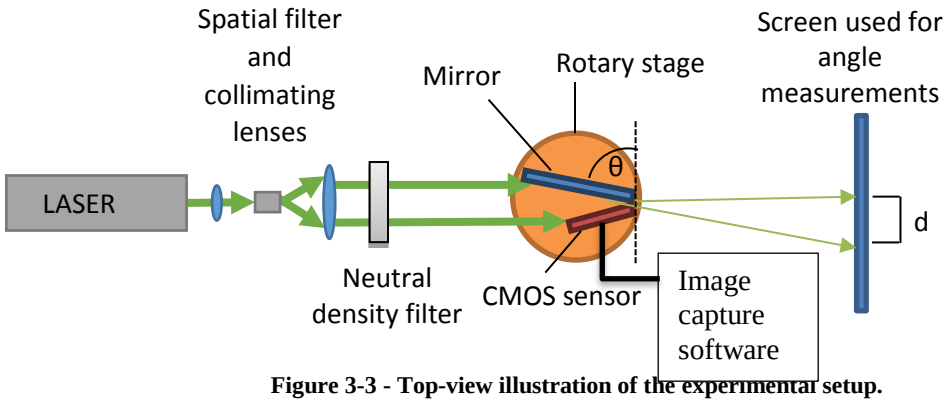

Figure 3-3 - Top-view illustration of the experimental setup.

The laboratory room was darkened and the stage, where the mirror/sensor assembly were located, was rotated until the heterodyne beat envelopes were clearly visible and as large as possible in the horizontal direction, when observed through the image capture software. The point of maximum horizontal beat pitch occurred several times throughout the rotation of the stage. A screen capture of the CMOS sensor was taken at each point and the distance *d* on the bypass screen was recorded so that the angle θ could be calculated. It will be explained later in the discussion that each of these positions correspond to the center of a dead zone, where the sensor cannot accurately measure the angle θ.

The rotary stage was set to the center of the first dead zone where the beat signal was strongest. It was then rotated clockwise in increments of approximately 0.1°. At each angle, a screen shot of the sensor output was taken and the value *d* was recorded in order to test the sensor's response curve and accuracy. This was done over a range of approximately 1.5° around the central dead zone until the heterodyne beats started to become too small for the sensor to resolve or until the signal started to deteriorate.

The color screen captures from the CMOS sensor were then separated into their RGB components and the G and B data was discarded. Only the red color information was retained, but the blue color information could have been equally used. The images were subsequently analyzed using the OriginPro software. Three randomly selected horizontal cross-sectional profiles were extracted from each image and the resulting profiles were curve-fitted with the equation $y = y_0 \left| sin\left(\pi \frac{x-xc}{\omega}\right)\right|$ in the OriginPro software to determine the value and uncertainty of ω, which corresponds to the pitch of a beat (in pixels). This value was then multiplied by the pixel array pitch of 4.2 μm to find Λ_{beat}. The beat pitch was then graphed

against the angle θ, which was calculated from the measured value of *d* from the bypassed light on the screen, and it was compared to the theory of the combined equations (1) and (2).

3.4 Results

Figure 3-4 contains images taken at the center of each dead zone at critical angles of θ where the horizontal pitch of the beat pattern approaches infinity. From equation (2), it can be concluded that this occurs when $\Lambda_L = \Lambda_S$. The sampling theory infers that the same condition can be met when $n\Lambda_L = \Lambda_S$ where *n* is an integer. Therefore, the images in Figure 3-4 correspond to the critical angles where Λ_L is a harmonic of Λ_S. The vertical components of the beat pattern, seen as alternating color bands in Figure 3-4, are due to the vertical off-normal misalignment between the mirror and sensor. As the angle θ was changed, the vertical component of the beat pattern stayed relatively constant throughout the stage rotation, as it is independent from the horizontal component of the beat pattern, which is only related to the angle θ. Therefore, the vertical alignment of the sensor is not critical in order to accurately measure rotations of the angle θ. Interestingly, the alternating vertical colors patterns of red and blue, and black and purple, are thought to be due to spatial crosstalk due to the large oblique angle when the light is striking the sensor. A theory on why each dead zone alternates between the various colors beat patterns is outlined in the discussion section.

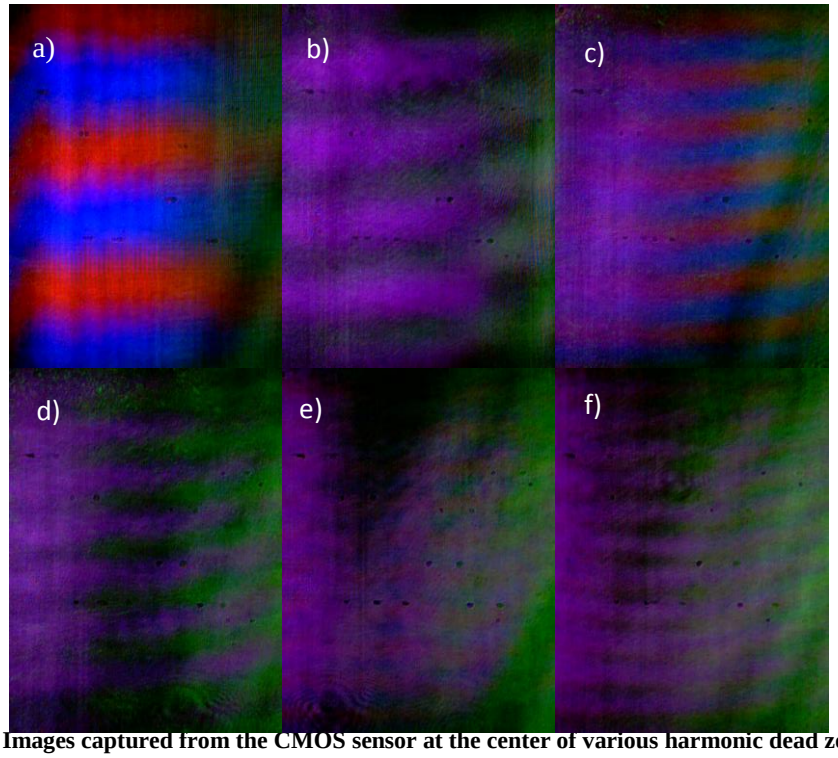

Figure 3-4 - Images captured from the CMOS sensor at the center of various harmonic dead zones. Inset a) corresponds to the first harmonic of a pair of pixels, b) the second harmonic, c) the third harmonic, and so on.

As the stage was rotated, the changing distance *d* on the bypass screen, seen in Figure 3-3, was measured and used to calculate the angle θ for each of the critical angles corresponding to the images in Figure 3-4. Equation (1) was then used to calculate the theoretical pitch of the light interference pattern (Λ_L) for each critical angle, using a constant mirror/screen angle $\phi = 39.8 \pm 0.2°$. The results are shown in

Table 3-2. These calculations demonstrate that the critical angles θ at the center of each dead zone create a light interference pattern that is harmonic to the double of pixel array pitch of 4.2 µm. Therefore, the value $\Lambda_S = 8.4$ µm corresponds to the spacing of a pair of pixels because the Bayer color pattern repeats every 2 pixels.

Table 3-2. The pitch of the light interference pattern at critical angles or dead zones.

Measured critical angle θ (deg)	Calculated pitch Λ_L using Eq. 1 (μm)	n^{th} harmonic	Calculated pitch multiplied by harmonic (μm)
87.172 ± 0.010	8.42 ± 0.04	1	8.42 ± 0.04
84.310 ± 0.011	4.19 ± 0.02	2	8.38 ± 0.04
81.474 ± 0.013	2.80 ± 0.01	3	8.41 ± 0.04
78.582 ± 0.015	2.099 ± 0.009	4	8.397± 0.036
75.704 ±0.017	1.683 ± 0.007	5	8.414± 0.036
72.782 ± 0.018	1.404 ± 0.006	6	8.423± 0.036

Figure 3-5 (a) is the greyscale representation of the red color portion of a screen capture from the CMOS sensor at the critical angle in the center of the dead zone from the 1^{st} harmonic and Figure 3-5 (b) is the corresponding horizontal cross-section from a random row from Figure 3-5 (a) with a fitted pitch ω of 492 ± 3 pixels. When the stage is rotated in small increments away from the center of the dead zone, the pitch of the horizontal component of the beat pattern becomes smaller while the pitch of the vertical component, related to the vertical mirror misalignment, stays the same. This results in a perceived tilt of the beat pattern, as seen in Figure 3-5 (c), which is the greyscale representation of the red portion of the screen capture at an angle of 0.17° away from the center of the dead zone illustrated in Figure 3-5 (a). Finally, Figure 3-5 (d) is the corresponding cross-section from a random row from Figure 3-5 (c) and it has a pitch ω of 34.36 ± 0.04 pixels. The uncertainty in the period of this curve fit is much lower than that in Figure 3-5 (b) because multiple beats can be measured and averaged by the curve fitting algorithm. The vertical misalignment of the mirror and sensor determines the direction of the angular displacement Δθ away from the center of the dead zone by the direction

of tilt. In this case, the counter-clockwise tilt of the interference pattern corresponds to a decrease in the angle θ of the device.

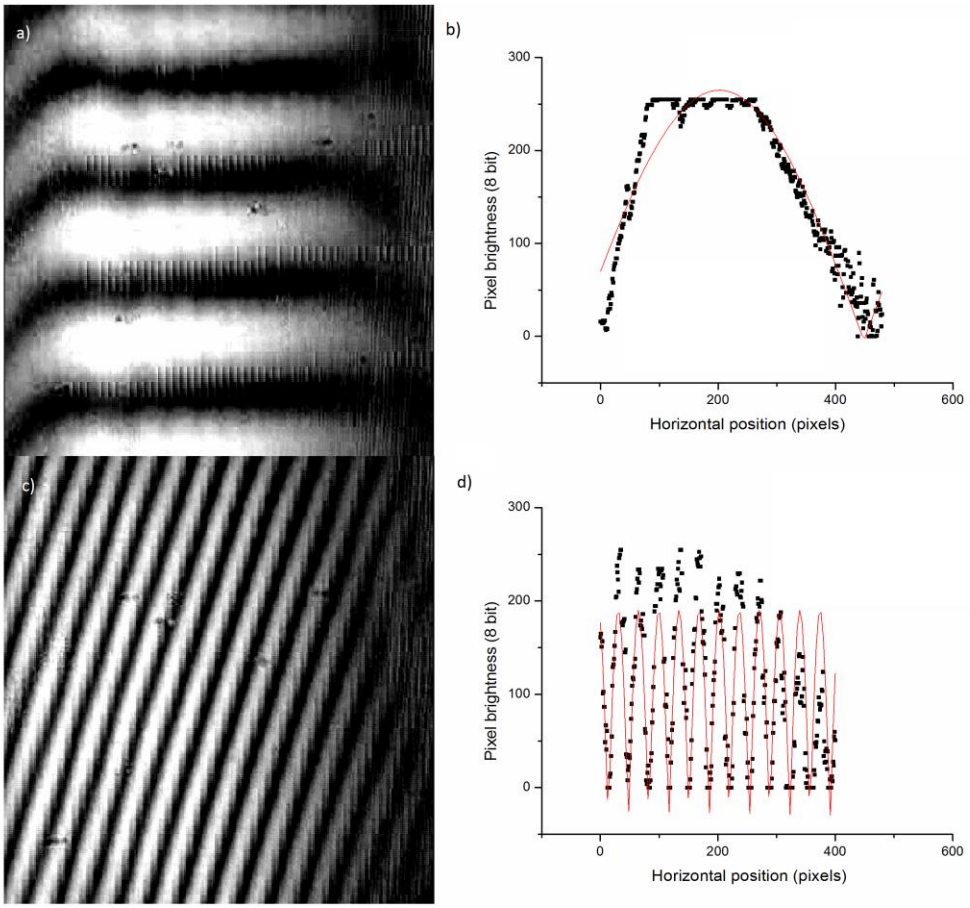

Figure 3-5 - Left: The red component of captured CMOS images. Right: The corresponding horizontal cross-section profile of a randomly selected row of pixels (dots) with curve fit (line). The top row corresponds to the center of a dead zone at an angle θ = 87.11 ± 0.01° while the bottom row, an angle of θ = 86.94 ± 0.01°.

The total uncertainty in the period of each beat envelope was calculated, using the Pythagorean theorem, by adding the random uncertainty from the results of 3 randomly selected rows to the average measurement uncertainty Δω from the curve fits. Each measured pitch (in pixels) was multiplied by the pixels array pitch of 4.2 μm and it was graphed in Figure 3-6 against the measured angle θ from the bypassed light screen. The red line in Figure 3-6 is the theoretical curve from combining equations (1) and (2) using an angle ϕ of 38.9° and its peak corresponds to the center of the sensor dead zone. As it can be seen, the experimental data agrees very well with the theory.

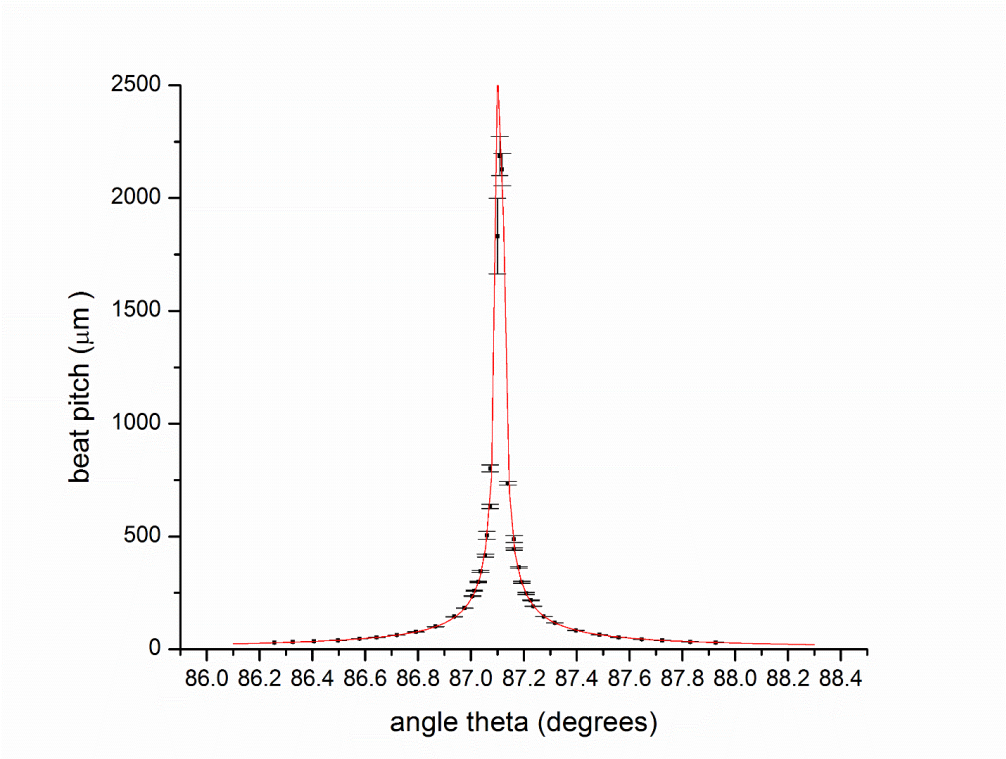

Figure 3-6 - The pitch of the imaged beat envelope versus the angle θ of the device centered on the critical angle of the 1st harmonic sensor dead zone. The Experimental data points are compared to the theory line from combining equations (1) and (2).

In order to estimate the accuracy of this angle measurement device, the theoretical sensitivity was multiplied by the total measurement uncertainty and it was graphed in Figure 3-7. The black line is the theoretical sensitivity, which is the derivative of the theoretical curve in Figure 3-6. The red line represents the total uncertainty of the curve fitting algorithm, which was obtained from the experimental data error bars in Figure 3-6. The accuracy of the angle measurement device is found by multiplying these two curves. The result is a fairly flat curve, shown in blue in Figure 3-7, with an average accuracy of $(9.2 \pm 0.9) \times 10^{-4}$ degrees or about 3.6 arcsec. Omitting the last two data points, the largest uncertainty of this curve is 8.9 arcsec.

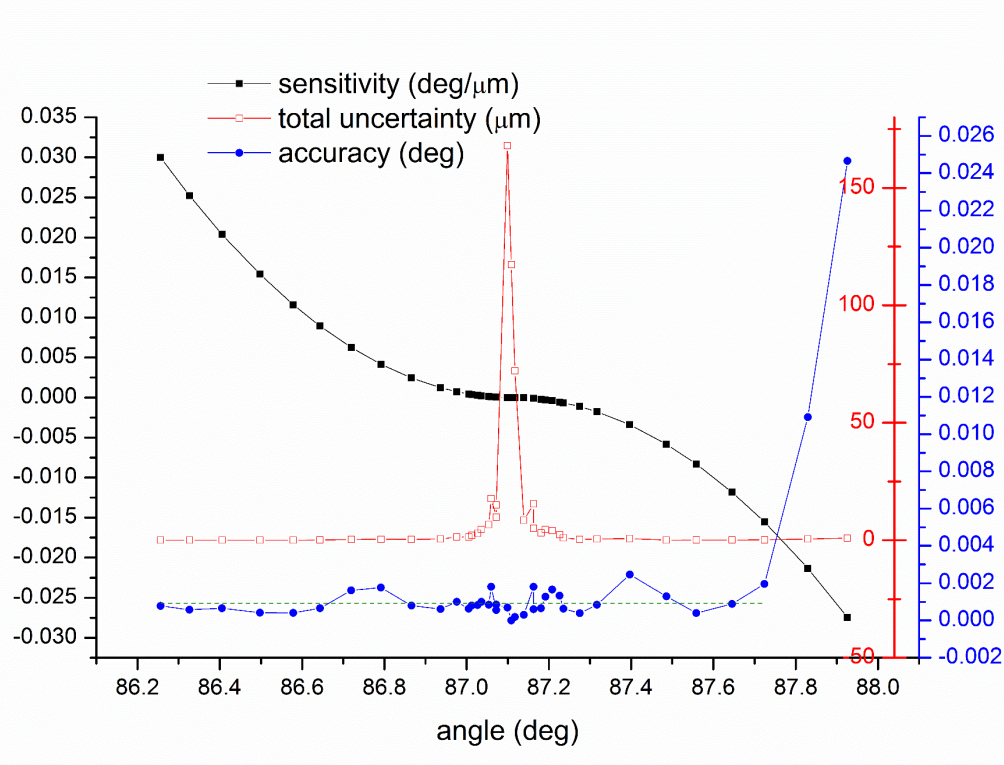

Figure 3-7 - A graph of the theoretical sensitivity, total measurement uncertainty of the beat pitch, and the accuracy of the device as a function of the angle θ centered on the critical angle of the 1st harmonic sensor dead zone.

Further testing was done to demonstrate that dual-axis angle measurements can also be performed using this device. Two mirrors projected two orthogonal interference patterns on the same CMOS sensor, as depicted in Figure 3-8. A custom fixture was used to hold the mirrors at an angle ϕ of approximately 93.5° to the CMOS sensor, while the incoming laser beam was set to be normally incident to the sensor. The mirror angles were measured as θ = 86.56° for the right-hand mirror and θ = 86.20° for the bottom mirror. Since this new fixture was only fixed temporarily, it was not possible to rotate the device to different angles θ. The resulting interference pattern can be seen in Figure 3-8. The angular position of the device resulted in a horizontal beat pitch of Λ_{beat} = 75.9 μm and a vertical beat pitch of Λ_{beat} = 93.5 μm. These values agree with the theory for an angle ϕ of 93.5° for both mirrors and a sensor pitch (Λ_S) of 4.2 μm. This demonstrates that it is possible to independently measure the two orthogonal light interference patterns for dual-axis angular measurements with a single sensor. The accuracy and sensitivity for this dual-axis device should theoretically be similar to the single-axis device presented earlier in this paper. However, additional uncertainty in the curve fitting may arise if the two signals are not perfectly orthogonal due to imperfect alignment.

There is no color crosstalk in Figure 3-8 because the light is close to being normally incident onto the sensor, so the CMOS is detecting the correct color of light.

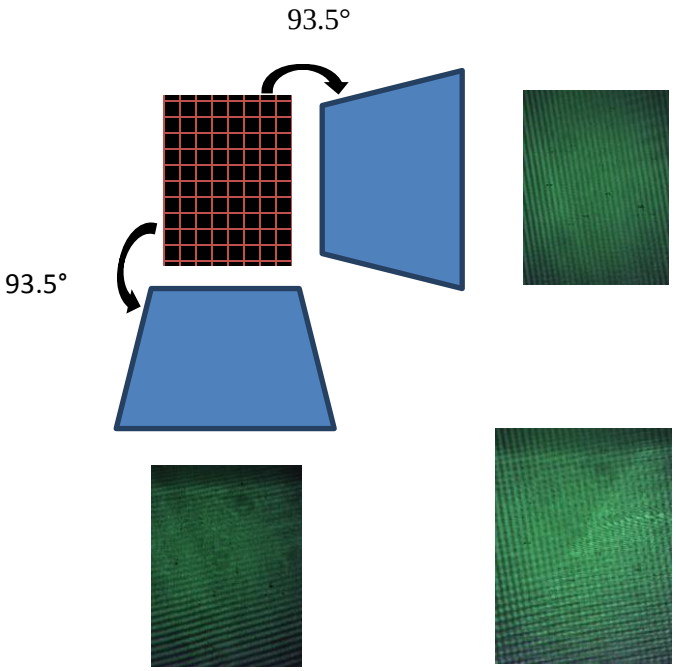

Figure 3-8 - Proof of concept testing for a dual-axis heterodyning optical angle measurement device. (Top left) is a diagram of the experimental setup where the beam of light is normally incident to the crosshatched CMOS sensor and is also incident on the two mirrors depicted in blue. (Top right) is the horizontal signal only with the light blocked to bottom mirror. (Bottom left) is the vertical signal only with light blocked to mirror on the right. (Bottom right) both vertical and horizontal signals are visible simultaneously when both mirrors and the sensor are illuminated.

3.5 Discussion

Figure 3-9 illustrates a proposed theory to explain the alternating color patterns, seen in Figure 3-4, by using the concept of spatial color crosstalk on a bayer-patterned sensor. Figure 3-9 (a) depicts the 1st harmonic when Λ_L is close to 8.4 µm or the size of one bayer-pattern element resulting in a pattern of red and blue beats. Figure 3-9 (b) depicts the 2nd harmonic when Λ_L is close to 4.2 µm or the size of one pixel which results in a pattern of purple and black. The left side of Figure 3-9 represents an arbitrary point on the sensor, while the center is some distance away where the phase shift of the light pattern is 180°, and finally, the right of this figure is the resulting image captured by the CMOS sensor. There are no triggered pixels in the center diagram of Figure 3-9 (b) because the particular phase and pitch of the interference

pattern is causing the light to periodically miss the photodiodes and strike the silicon substrate, as illustrated in Figure 3-1. It is worth noting that the experiment uses an older generation VGA CMOS sensor from the mid-2000s. It is possible that newer CMOS sensors will not produce the same color crosstalk results because of advances in CMOS sensor architecture. The color crosstalk, although initially unexpected, does have an advantage. Since the source laser beam is green (wavelength of 532 nm), and since the sensor signal is blue or red, the signal can be easily filtered by color separation. By removing the unwanted green color portion from the screen capture, a large portion of the ambient light noise is removed. Although the device was tested in a darkened room, further experimentation with a higher laser irradiance and a band pass filter at 532 nm may allow it to function in environments with higher levels of ambient light.

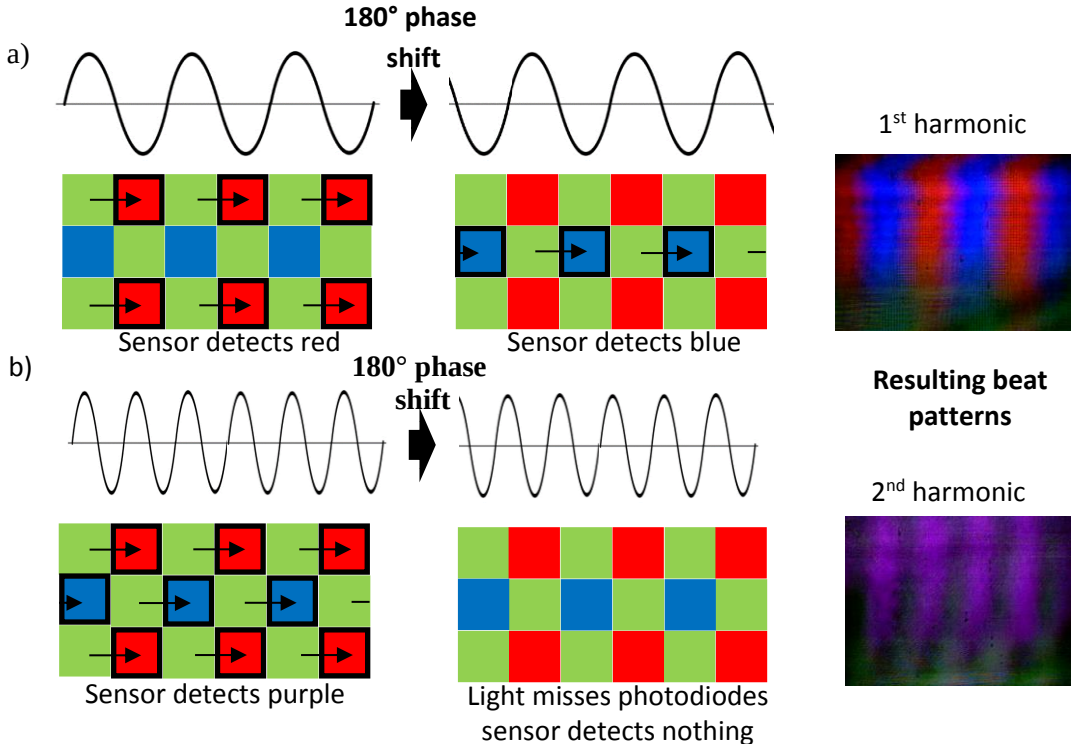

Figure 3-9 - An interference pattern of green light with a periodic amplitude (represented by the black sinusoidal wave) is projected on the bayer-pattern CMOS sensor (represented by the colored squares) at an oblique angle such that color crosstalk occurs (illustrated as black arrows). Activated pixels are represented as one with bold black outlines.

A minor image distortion was observed on the left side of Figure 3-5 (a) where the beat patterns seem to curl downward. Additionally, the right side of both screen captures in Figure 3-5 tends to get darker as the amplitude of the pattern decreases. These distorted profiles

contribute to the uncertainty of the curve fitting results, especially near the dead zone angles where the beat envelope is very large. In theory, the profile of the horizontal cross-section at the center of a dead zone should be perfectly flat. However, the deformation on the left and the lower amplitude on the right of the image creates a false envelope. The result is that the curve fitting algorithm greatly underestimates the value and uncertainty of ω in the sensor dead zone. The error bars near the peak of the curve in Figure 3-6 are therefore artificially small. These erroneous uncertainties are multiplied by the theoretical sensor response in Figure 3-7, which is why the loss of accuracy in the dead zone is not represented in this figure. The uncertainty of the angle measurements should be much higher around the central critical angle. The curve fit in Figure 3-5 (d) shows none of these systemic errors demonstrating that the sensor is operating with optimal accuracy outside of the sensor dead zone.

Cropping of the left and right sides of the image before curve fitting may help eliminate some of the systemic error caused by the edge distortions. If it is estimated that pixels between the 50^{th} column and the 400^{th} column are not distorted and the image is cropped between those points, that leaves 350 pixels or 1470 μm of usable sensor width. If a measured beat envelope pitch Λ_{beat} smaller or equal to 1470 μm is required to stay outside of the sensor dead zone, then the theory gives a dead zone angular span of ± 0.0165° or roughly 1 arc minute on either side of the critical angle $\theta = 87.1095°$.

The best way to improve the sensor performance would be to increase the physical size of the CMOS sensor, which has two main advantages: Firstly, the dead zones would be smaller since the larger sensor will allow a more accurate estimate of the pitch of larger beat envelopes. Secondly, the overall sensor accuracy will increase for the whole range of the sensor because the curve fitting algorithm will have a longer baseline and a greater sample size. Decreasing the pixel size and spacing on the CMOS would not increase the accuracy of the instrument, but it would increase its theoretical range since the higher spatial sampling rate would allow detection of smaller pitches of beat envelopes further away from a dead zone. Even if the sensor is larger, there still must be a good quality light interference pattern projected onto it. This may be the practical limiting factor on the accuracy of this device, as seen by the image distortions in Figure 3-5, although the absolute cause of the image distortions in this experiment is not known. They could be from edge effects of the light hitting the side of the sensor at an oblique angle or from imperfections in the flatness of the sensor or mirror. Further work could involve testing different CMOS sensors and geometries to reduce the image distortions and it may improve the range and accuracy of this angle measurement device.

3.6 Conclusion

An optical angle measurement device has been tested and shown to have an accuracy better than 8.9 arc sec over a range of 1.47° with a dead zone of 1.9 arcminutes in the center of its measurement range. Although not as accurate as some currently available optical angle measurement devices, the proposed device does have major advantages. It is extremely simple and inexpensive, as it was made up of components from a $10 web camera and a small mirror. Furthermore, this device requires a low-power laser light with an irradiance of only 20 mW/m^2. The color crosstalk phenomenon makes it easy to verify the signal integrity and filter ambient noise. The measurement device is relatively small and it can be easily mounted externally to an object to measure its orientation in free space. All angle measurements can be made in situ without the need for external sensors. With a small integrated computer, it would be possible to perform the image processing, curve fitting, and real time angle calculations onboard the device itself. The optical spatial heterodyning of the interference pattern with the CMOS pixel spacing increases the sensitivity of the sensor over a relatively large range of angles. The angle measurements are absolute rather than relative, which means there is no loss of accuracy over time due to drift. The proposed sensor can have multiple orientations that produce heterodyne signals due to the different possible harmonics of the sensor pitch. Lastly, a proof-of-concept test has demonstrated that it is possible to perform dual-axis angle measurements with a single CMOS sensor.

References

[60] Belrose, J. S., "Fessenden and Marconi: Their differing technologies and transatlantic experiments during the first decade of this century," Proceedings of the 1995 International Conference on 100 Years of Radio, 32-43 (1995).

[61] Armstrong, E. H. , "The super-heterodyne-its origin, development, and some recent improvements," Proceedings of the Institute of Radio Engineers 12(5), 539-552 (1924).

[62] Protopopov, V. V., [Laser Heterodyning], springer (2009).

[63] Lawler, J. E., Labby, Z. E., Harlander, J. M. and Roesler, F. L. , "Broadband, high-resolution spatial heterodyne spectrometer," Appl.Opt. 47(34), 6371-6384 (2008).

[64] Kojima, T., Kikuchi, Y., Seki, S. and Wakiwaka, H., "Study on high accuracy optical encoder with 30 bits," The 8th IEEE International Workshop on Advanced Motion Control, 2004. AMC'04., 493-498 (2004).

[65] Yuan, J. and Long, X. , "CCD-area-based autocollimator for precision small-angle measurement," Rev.Sci.Instrum. 74(3), 1362-1365 (2003).

[66] Chapman, G. , "Interferometric angular measurement," Appl.Opt. 13(7), 1646-1651 (1974).

[67] Ikram, M. and Hussain, G. , "Michelson interferometer for precision angle measurement," Appl.Opt. 38(1), 113-120 (1999).

[68] Zhang, A. and Huang, P. S. , "Total internal reflection for precision small-angle measurement," Appl.Opt. 40(10), 1617-1622 (2001).

[69] Guo, J., Zhu, Z. and Deng, W. , "Small-angle measurement based on surface-plasmon resonance and the use of magneto-optical modulation," Appl.Opt. 38(31), 6550-6555 (1999).

[70] Srikanth, G. , "Measurement of period of interference patterns with sub-micron period," Optics & Laser Technology 39(5), 918-921 (2007).

[71] Hochberg, E. B. and Chrien, N. L., "Lloyd's mirror for MTF testing of MISR CCD," Optical Spectroscopic Techniques and Instrumentation for Atmospheric and Space Research II, 274-285 (1996).

[72] Kaymak, Y., Rojas-Cessa, R., Feng, J., Ansari, N., Zhou, M. and Zhang, T. , "A survey on acquisition, tracking, and pointing mechanisms for mobile free-space optical communications," IEEE Communications Surveys & Tutorials 20(2), 1104-1123 (2018).

[73] Suhr, J. K., Jung, H. G., Li, G. and Kim, J. , "Mixture of Gaussians-based background subtraction for Bayer-pattern image sequences," IEEE Transactions on Circuits and Systems for Video Technology 21(3), 365-370 (2010).

[74] Agranov, G., Berezin, V. and Tsai, R. H. , "Crosstalk and microlens study in a color CMOS image sensor," IEEE Trans.Electron Devices 50(1), 4-11 (2003).

[75] Leibold, J. and Sabat, R. G. , "Fabrication of micrometer-scale surface relief gratings in azobenzene molecular glass films using a modified Lloyd's mirror interferometer," Optical Materials 96, 109315 (2019).

CHAPTER 4: Inline holographic inscription of diffractive lenses in azobenzene molecular glass thin films

Abstract

A simple inline holographic setup is used to fabricate holographic diffractive lenses using off-the-shelf components. The resulting surface relief gratings are inscribed directly in azobenzene-functionalized thin films with pitches that agree well with a theoretical Fresnel zone plate. The annular gratings have an outer radius of approximately 9 mm and an inner radius of less than 4 mm. Interfering laser beams, circularly polarized in the same direction, generally produce poor-quality gratings in azo-films, but the addition of a reference beam lens greatly improved their consistency and produced quality gratings with depths up to 400 nm. Multiple exposures produce multi-focal diffractive lenses, while angling the sample resulted in focal lines, instead of focal points.

4.1 Introduction

A diffractive lens is a diffractive optical element (DOE) that focuses light using diffraction instead of the more traditional refraction. Diffractive lenses normally suffer from dispersion and are generally not as efficient as their refractive counterpart, however they are much thinner in design and use less material [76]. The result is an optical element that is smaller and lighter and may be used in the miniaturization of optical technologies such as photonic lab-on-a-chip devices [77], chip-based lasers [78], communication devices such as optical interconnects [79], ultra-thin cameras [80], solar cell concentrators [81] and beam shaping devices [82]. One disadvantage for DOEs is that the diffraction patterning, at scales as small as hundreds of nanometers, can be time consuming and expensive to manufacture. Gates *et al* [83] provide a good overview of the main categories of common nanofabrication techniques that could be used to manufacture DOEs including photolithography, scanning beam lithography, hard or soft molding or embossing, micro contact printing, scanning probe lithography, edge lithography, and self-assembly methods. In particular, interference lithography (IL) offers several advantages over other nanofabrication techniques because it has the inherent high production rate of photolithography, and can produce continuous phase gratings in a single step process without the need for a photomask. Holographic lenses are a subset of diffractive lenses that are made by using IL fabrication techniques. The most common types of holographic lenses are asymmetrical and are created using off-axis Leith and Upatnieks holographic setup

where the image beam and reference beam are not co-linear [84]. Like all off-axis holograms, these asymmetrical holographic lenses benefit from an angular separation between images created by the various diffractive orders, resulting in holographic images with less background noise. Symmetrical holographic lenses are fabricated as inline Gabor-type holograms where the reference and object beams have the same optical axis [85]. The resulting symmetric holographic lens can be compared to a Fresnel zone plate (FZP) which is the original diffractive lens based on the analysis of Augustin-Jean Fresnel in 1866 [86]. These symmetrical holographic lenses do suffer from multiple focal points on the same optical axis as well as chromatic aberration, however these disadvantages may be compensated for or even exploited using specialized inline optical systems such as confocal microscopes [87], UV telescopes [88], and other specialized holographic imaging techniques [89].

In 1995, it was discovered that thin films of an azobenzene-functionalized polymer display a photomechanical effect allowing for the production of surface relief gratings (SRG) by exposing them to a laser interference pattern [90]. Many mechanisms for this photomechanical effect have been proposed, most theories are based on the well-known *trans-cis* photo-isomerization of the azobenzene molecules [91]. A known experimental result is the dependency of the grating formation on the polarization of the interfering beams [92]. However, the use of azobenzene-functionalized materials as a photoresist is advantageous in that it allows for a single-step fabrication process of the interference pattern in surface relief without the need for any additional etching. Our research group had previously published a method of fabricating symmetrical chirped-pitch circular gratings using a custom fabricated mirror fixture [93]. The fabrication method for annular gratings presented here offers several advantages in that it uses only off-the-shelf optical elements and the resulting annular gratings are designed to focus light. Other examples of holographic lenses on azobenzene-functionalized materials in literature include off-axis lenses made using a Lloyd's mirror interferometer [94] and bifocal off-axis lenses made using different pitches for volumetric and surface gratings [95]. This paper describes a novel inline holography approach to manufacturing annular FZPs in surface relief on azobenzene-functionalized thin films. The experimental setup is extremely simple using commercially available components without the requirement for multiple laser beam paths or beam splitters. This method can be used to quickly and inexpensively manufacture functioning inline holographic lenses for research in the fields of optics and plasmonics.

4.2 Theory

In a previous paper [96], from geometric optics, we detailed the equation,

$$\Lambda = \frac{\lambda}{\left|\cos(\alpha_1) - \cos(\alpha_2)\right|} \tag{9}$$

to find the pitch Λ of an interference pattern projected onto a sample. The periodicity of the sinusoidal light pattern is determined by the wavelength of light λ and the angles of the two interfering beams α_1 and α_2, as seen in Figure 4-1 (a). The geometric basis of a holographic lens is depicted in Figure 4-1 (b) as 2-point sources of light O and R depicting the object and the reference points at distances *u* and *v* respectively from the sample. The geometry for a certain height *x* from the optical axis on the sample uses the equations $\alpha_1 = \tan^{-1}(u/x)$ and $\alpha_2 = \tan^{-1}(x/v) + \pi/2$ which can be substituted into Eq. (1) and simplified to give $\Lambda = \lambda / x\left(\sqrt{1/(u^2 + x^2)} + \sqrt{1/(v^2 + x^2)}\right)$. Assuming the paraxial approximation where $x \ll u$, $x \ll v$ and rearranging gives,

$$\Lambda = \frac{\lambda uv}{x(u+v)} \tag{10}$$

This equation describes the pitch of a FZP as a function of distance *x* from the center. It may be proven that the resulting hologram is a FZP by taking the known equation for the radius x_n of the *n*th fringe of a FZP with focal length *f*, $x_n^2 / 2f = n\lambda$ [85], isolating for x_n, taking the derivative with respect to *n*, substituting the definition of *n* from the original FZP equation and substituting the focal length from the thin lens equation, which gives: $dx/dn = \lambda uv / x(u+v)$ where *dx/dn* is the change in the radius per fringe which is equivalent to the pitch Λ of the grating at point *x* in Eq. (2). For the special case of a FZP where the reference beam is a plane wave, *v* approaches infinity and we get the equation:

$$\Lambda = \frac{\lambda u}{x} \tag{11}$$

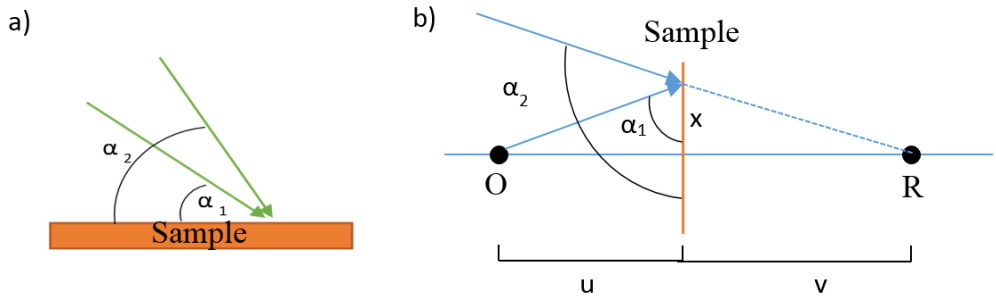

Figure 4-1 - (a) A thin film of azobenzene-functionalized material is exposed to two beams of interfering light at angles α_1 and α_2. (b) The geometric basis for a holographic Fresnel Zone Plate depends on the wavelength of inscribing light and the distance of the object (O) and reference (R) point sources of light.

4.3 Experiment

Soda lime microscope slides were cleaned and spin coated with a 3% solution by weight of azobenzene Dispersed Red 1 (DR-1) functionalized molecular glass [97] in dichloromethane to create solid thin films with roughly 600 nm thickness. A sample slide was then placed in the experimental set-up as shown in Figure 4-2 (a). The beam from a Coherent Verdi V6 laser with a wavelength of 532 nm was made circularly polarized with a quarter wave plate so that there would not be any directional dependence for the formation of circular grating lines. The beam was then focused and passed through a spatial filter to remove unwanted lobes and expanded with a collimator. A small object lens with a diameter of 9.7 mm and a focal length of 5 cm was suspended in the center of the beam using a single thin wire at a distance of u = 13.4 cm between the focal point and the sample. The sample was exposed to the laser beam with measured irradiance of 0.82 W.cm^{-2} for 1000 seconds. The experiment was repeated with the addition of a large plano-convex reference beam lens with focal length of 35 cm and thickness of 1.5 cm as shown in Figure 4-2 (b) with u = 11.5 cm and v = 25.5 cm. The same experimental set-up as Figure 4-2 (b) was repeated, but with the sample rotated 45 degrees from normal incidence of the light beam. Finally, multiple exposures with the reference lens at different distances from the same sample were made, the first exposure was 1000 seconds long with u = 20 cm and v = 16.5 cm, the second one was 300 seconds long with u = 20 cm and v = 11.5 cm, in order to test the fabrication of a diffractive lens with multiple focal points. Previous work on superimposed gratings in our lab has shown that a reduced exposure time to inscribe a second grating is beneficial so as not to overly degrade the first grating [98]. The pitch and depth of the resulting annular gratings were measured using a Bruker Dimension Edge Atomic Force

Microscope (AFM). The annular gratings were then placed on an optical table in the path of a collimated and expanded beam of light from a Helium-Neon laser. A high-dynamic range monochromatic CCD camera on a staged motor was moved along the optical axis in order to find the focal points of the fabricated DOEs. A Gaussian curve was fit to a cross section of the image through the focal point and the full width half maximum (FWHM) of the peak was determined. The relative diffraction efficiency was measured using a collimated and expanded probe laser at 632.8 nm passing through a mechanical chopper, then through the sample and onto a photodiode hooked up to a lock-in amplifier. The 1st order relative diffractive efficiency was calculated by dividing the photodiode signal of the light passing through a circular hole sized to the focal point of the holographic lens by the total beam photodiode signal passing through a flat section of the azobenzene thin film sample.

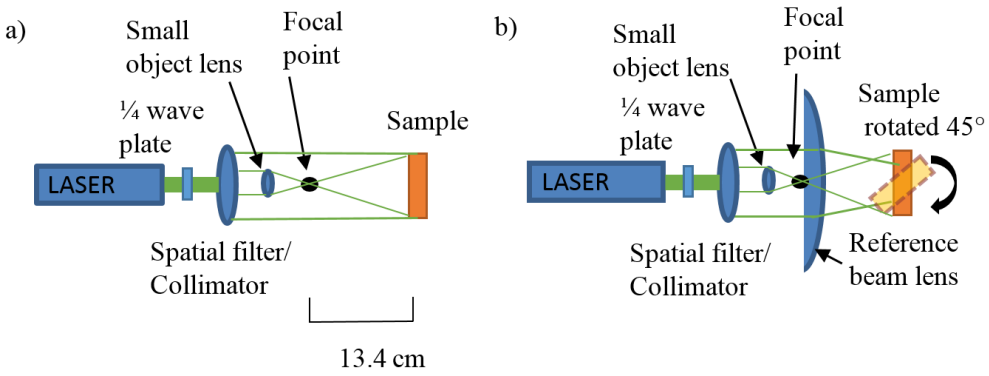

Figure 4-2 (a) Experimental set-up for production of inline holographic lens with planar reference beam. (b) Experimental setup with reference beam lens added for production of inline holographic lens with a converging reference beam. The sample was also canted approximately 45 degrees in a separate trial.

4.4 Results

The annular diffraction gratings fabricated using the single object lens shown in Figure 4-2 (a) had a maximum measured grating modulation depth of 126 nm, but the depth of the gratings was very inconsistent depending on the azimuthal position on the sample. Because of the poor circular symmetry of the grating formation, no focal points were visible from this sample. Despite the inconsistent depth, pitch measurements as a function of radial distance from the center agreed well with the theory in Eq. (3), as seen in Figure 4-3.

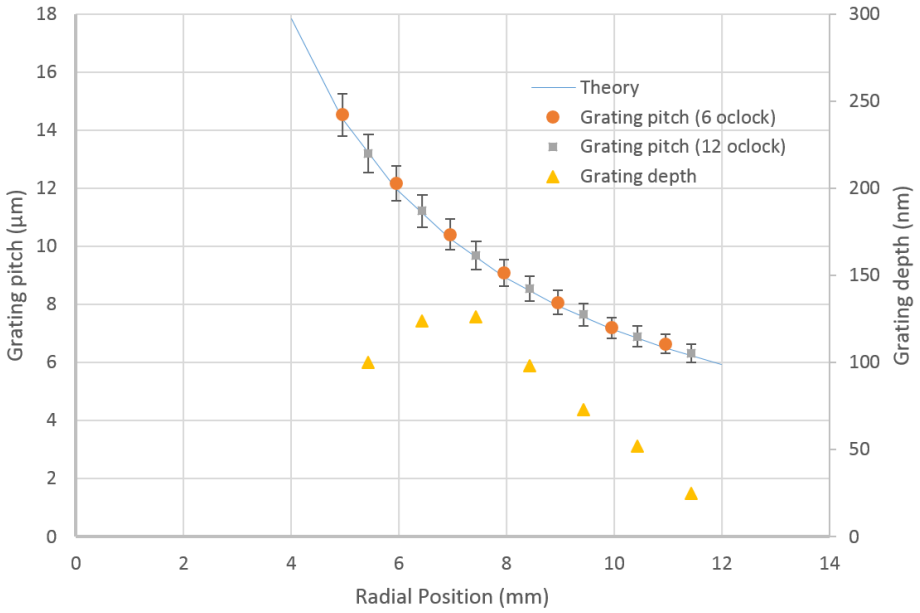

Figure 4-3 - Grating pitch and depth as a function of radial distance from center of holographic lens fabricated using a single object lens with focal point 13.4 cm from sample (*u* = 13.4 cm) and planar reference beam. Data points were taking at opposite sides of the sample at the 12 o'clock and 6 o'clock positions to test for symmetry. Although measurements at the 12 o'clock orientation resulted grating depths of up to 126 nm, other orientations had grating depths of less than 10 nm resulting in an inefficient diffractive lens.

When the second large reference beam lens was added to the experimental set-up shown in Figure 4-2 (b), the resulting gratings were much deeper, with maximum measured modulation depths of more than 400 nm. The gratings were very regular as seen in Figure 4-4 and consistent for all azimuthal positions except at the 12 o'clock position where the wire suspending the small object lens casts a shadow on the interference pattern.

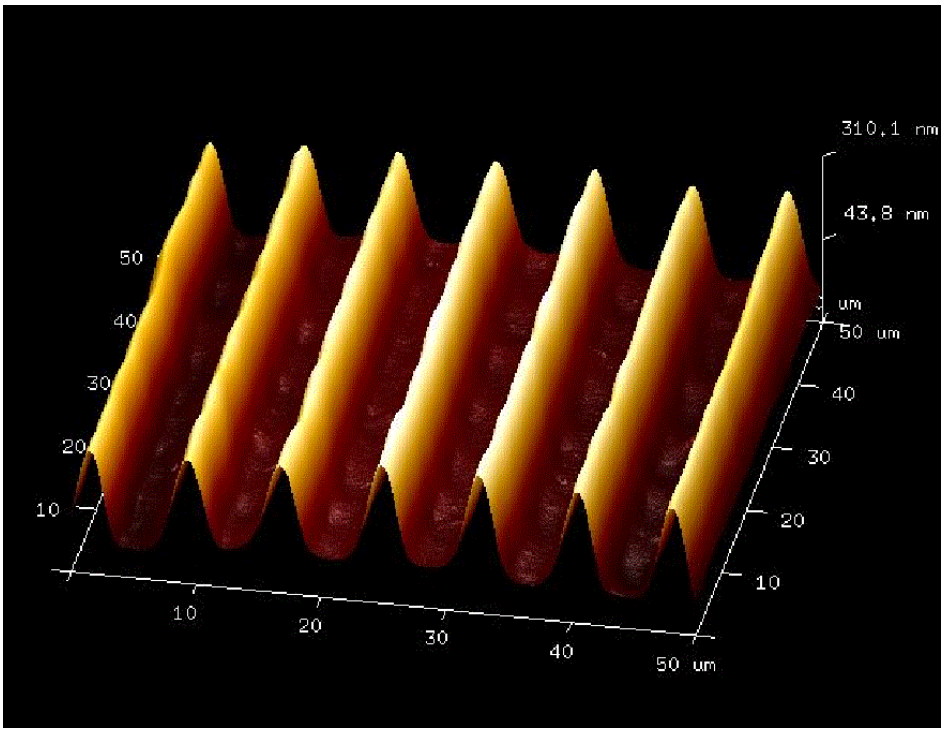

Figure 4-4 - Surface profile AFM measurements of holographic lens using converging object lens and reference lens.

The measured grating pitch in relation to the radial distance matched the theory of a FZP in Eq. (2) very well as seen in Figure 4-5. In order to verify the validity of the paraxial and thin lens approximations used in the theory, a ray trace simulation was performed with a reference lens thickness of 1.5 cm. The results match well to the FZP theory and are included in Figure 4-5. The sample was tested for its ability to focus monochromatic collimated light at 632.8 nm wavelength. A first order focal point was detected 6.5 cm from the sample and a second order focal point at 3.2 cm from the sample, as seen in Figure 4-6. These focal distances agree with the predicted focal points based on the pitch and position of the annular gratings. A relative diffraction efficiency of 8.5% was measured at the 1st order focal point with a FWHM of 148 μm.

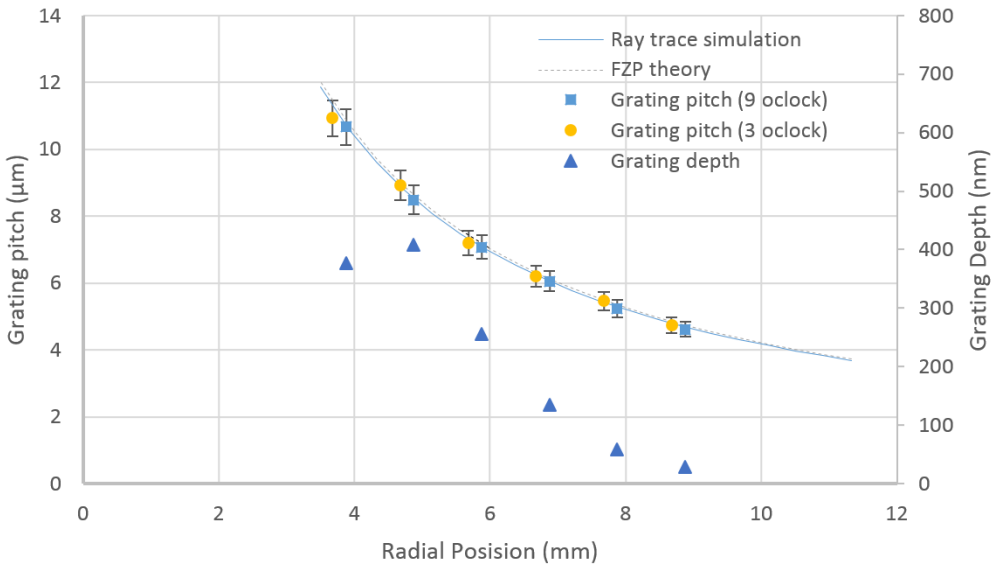

Figure 4-5 - Grating pitch and depth as a function of radial position from center of holographic lens fabricated using an object lens with focal point 11.5 cm from the sample (*u* = 11.5 cm) and a reference lens with focal point 25.5 cm behind the sample (*v* = 25.5 cm). Data points were taking at opposite sides of the sample at the 3 o'clock and 9 o'clock positions to test for symmetry.

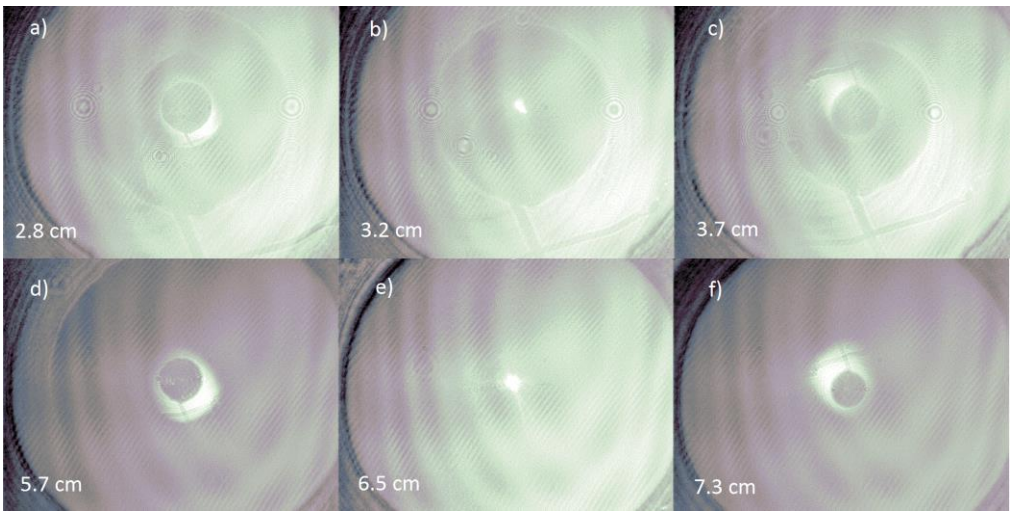

Figure 4-6 - Photographs of light focalization at different distances from the camera to the sample using a collimated light source with a wavelength of 632.8 nm. Inset images e) and b) represent the first order and second order diffraction focal points, respectively, as predicted from the diffraction grating equation. All focal points are on the optical axis because of the in-line holographic setup used.

When the sample was rotated 45 degrees from normal incidence as shown in Figure 4-2 (b), circular symmetry of the grating is lost and an elliptical grating is produced with larger measured pitches in the horizontal direction than the vertical direction. When tested for

focalization, this vertical and horizontal symmetry created alternating vertical and horizontal focal lines as seen in Figure 4-7.

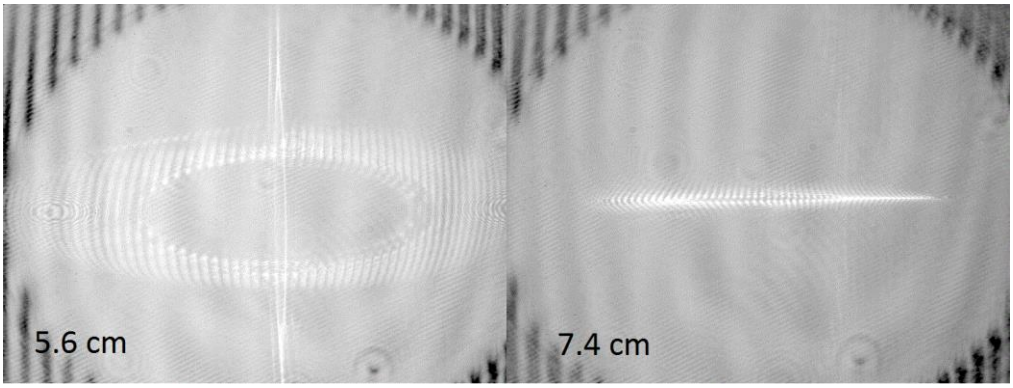

Figure 4-7 - Vertical (left) and horizontal (right) focalization lines created by canting the incident angle of the sample in the holographic set-up. Distances from sample to camera are shown for a sample illuminated with a collimated laser with a wavelength of 632.8 nm.

When multiple holographic exposures were made on the same sample, the superimposed pitches were close enough to create a beat interference pattern shown in Figure 4-8 (top). This made it difficult to measure the pitches of the two superimposed gratings directly, but a Fourier analysis of the modulation profile made it possible to estimate the two pitch values on the sample, as seen in Figure 4-8 (bottom). The annular gratings were very deep and regular with maximum depths approaching 600 nm. The measured pitch as a function of distance from the center of the grating match well with the theory for the two different exposures as shown in Figure 4-9. The sample showed multiple focal points as a result of the different diffraction orders of the two superimposed pitches as seen in Figure 4-10. A relative diffraction efficiency of 7.1% was measured at the 1st order focal point of the primary grating with a FWHM of 277 μm and a relative diffraction efficiency of 1.9% with FWHM of 158 μm was measured for the 1st order focal point from the secondary grating fabricated by the second exposure.

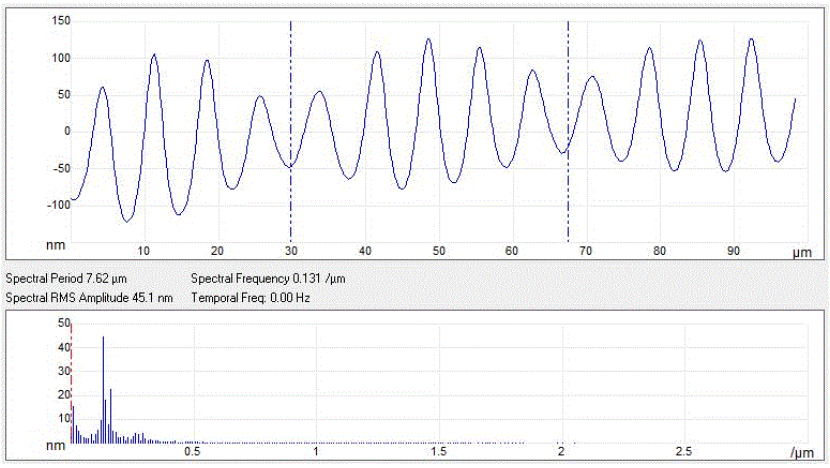

Figure 4-8 - Grating profile measurement from AFM (top) with Fast Fourier Transform (bottom) of sample that was exposed to two different holographic lens geometries. The superimposed grating pitches of 7.6 µm and 6.3 µm interfere to create a beat envelope pattern.

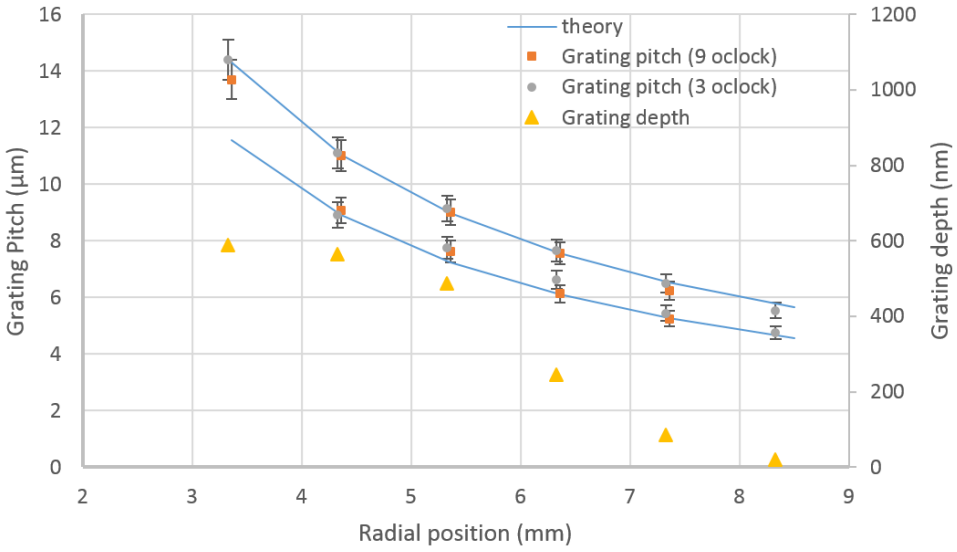

Figure 4-9 - Grating pitch and depth as a function of distance from center on a sample with two superimposed exposures. The top line corresponds to the theory of a FZP with *u* = 20 cm and *v* = 16.5 cm. The bottom line corresponds to the second exposure where the large reference mirror was moved 5 cm to create a theoretical FZP with *u* = 20 cm and *v* = 11.5 cm. Data points were taking at opposite sides of the sample at the 3 o'clock and 9 o'clock positions to test for symmetry.

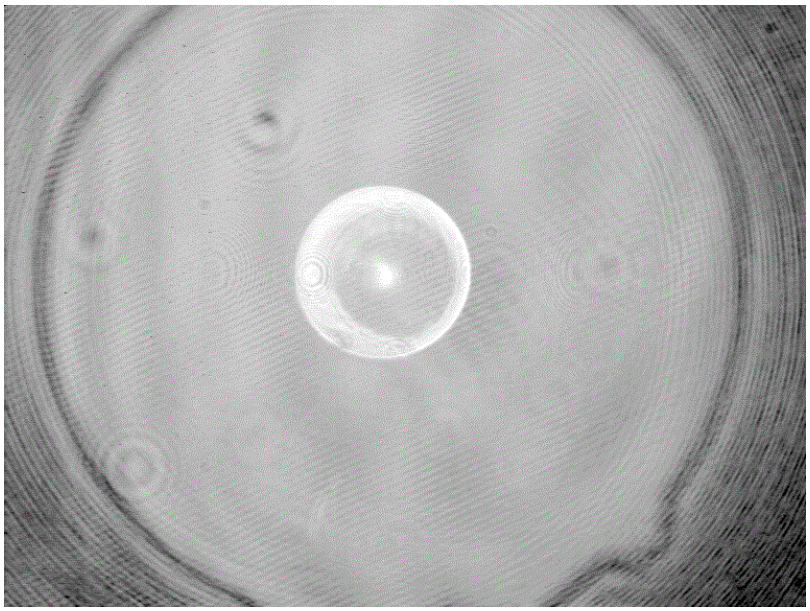

Figure 4-10 - Multiple focal points are present on a single sample of superimposed holographic lenses. The focal point in the center corresponds to a focal length of 6.1 cm from the second exposure, while the ring of light corresponds to a focal length of 7.6 cm from the first exposure. The image was created using a collimated light source with a wavelength of 632.8 nm.

4.5 Discussion

One limitation of this manufacturing method for holographic lenses is the fact that the small object lens casts a shadow in the reference beam at center of the sample which results in the formation of annular gratings instead of a complete circular FZP. Using the matrix method for paraxial optics, it was calculated that the outer radius of the object beam, r_{outer}, at the sample is,

$$r_{outer} = r_{ol}\left(-\left(L_1\left(1-0.0286L_4\right)+0.9714L_3+1\right)/\ f_{ol}-0.0286L_3+1\right) \tag{12}$$

Where r_{ol} is the radius of the small object lens, L_1 is the distance from the object lens to the reference lens, L_3 is the distance from the reference lens to the sample and f_{ol} is the focal length of the object lens. This was calculated using an index of refraction of 1.5 for the lenses and the radius of curvature of -17.5 cm and thickness of 1.5 cm for the plano-convex reference lens. In order to optimize the area of the holographic grating, the radius of the collimated beam from the laser, r_{beam}, must be large enough so that the reference beam is the same size as the object beam, r_{outer}, at the sample. The minimum r_{beam} can be calculated as,

$$r_{beam} = r_{outer}\ /\ (1-0.0286L_3) \tag{13}$$

to ensure that the object and reference beams overlap. The inner radius of the holographic sample from the object beam, r_{inner}, can likewise be calculated as,

$$r_{inner} = r_{ol}(1 - 0.0286L_3) \tag{14}$$

For the experimental setup shown in Figure 4-5 and given the parameters, L_1=7 cm, L_3=9.5 cm and f_{ol}=5 cm, Eq. (4) can be used to calculate a r_{outer} of 1.16 cm, and Eq. (6) an r_{inner} of 0.36 cm. Likewise Eq. (5) can be used to find a minimum required collimated output beam radius r_{beam} of 1.59 cm. Comparing these parameters to Figure 4-5 shows that the theoretical r_{inner} is quite close to the actual experiment. However, at a distance of r_{outer} from the center of the sample, the depth of the annular SRGs is too small to make good measurements. This is because the grating depth decreases farther from the center of the sample. For example in Figure 4-5, the furthest data point was approximately 8.9 mm from center and it had a depth of only 29 nm. This is likely because the weaker irradiance around the outside edges of the Gaussian profile of the reference beam reduces the interference contrast with the object beam.

The relatively low diffraction efficiency of these holographic lenses is in part due to the multiple diffractive orders observed and because of the virtual (diverging) and real (converging) focal points of the lenses. The annular nature of the FZPs will also reduce their ability to collect and focus light when compared to a full circle zone plate. The diffractive lenses fabricated in this paper will not be able to compete with high efficiency FZP such as blazed diffractive optics that are capable of diffraction efficiencies approaching 100% [99]. However, for applications that require light in certain regions to pass through unimpeded, such as solar concentrators, the annular shape FZP may be advantageous [100].

Another interesting result is the fact that the addition of a second lens in the reference beam path greatly improved the depth and quality of the manufactured gratings. Literature reports that two interfering beams having the same direction of circular polarization are very inefficient at creating SRGs in azo-polymer thin films while two circularly polarized beams having opposite handedness are optimum [101]. Circularly polarized light was chosen for this experiment because of the circular symmetry of the set-up required a non-directional polarization as opposed to the linear polarized light from the laser source. It is not surprising that the single lens experiment produced lesser quality gratings since the reference and object beams were both left-hand circularly (LHC) polarized. It is hypothesized that the addition of the large reference beam lens tilts the electric field of the reference beam slightly in the p-

polarization direction causing a reduction of the vector magnitude in this direction. This results in an elliptical polarization for both the object and reference beam that still maintains the circular symmetry required to form a uniform annular grating. It is possible that the addition of a custom-made half-wave plate having the same size as the small object lens and placed directly in front of it, would increase the grating formation efficiency by switching the handedness of the object beam for the optimum polarization configuration. However, in the interest of using off-the-shelf optical components, the use of the reference beam lens provides excellent results and is a key component of the experimental set-up.

The flexibility of this fabrication method is demonstrated in Figure 4-7 and Figure 4-10, where modifying the geometry of the experiment and by using multiple exposures allows for the creation of unique DOEs that are analogous to cylindrical or circular lenses with multiple focal points. Although each focal point has a lower diffraction efficiency, multifocal lenses have previously been designed and tested for applications such as beam splitting [102] and ophthalmology [103]. Other refractive optical elements such as axicons or other beam shaping elements could be used instead of the object lens to produce other customized DOEs.

4.6 Conclusion

Symmetrical diffractive lenses were fabricated in surface relief on thin films of azobenzene-functionalized glass-forming material for the first time using a Gabor inline holographic set-up. The pitch of the resulting annular gratings matched the theory for a Fresnel zone plate with a high degree of accuracy and the resulting samples focalized monochromatic light at predictable focal points with relative diffraction efficiencies of up to 8.5 %. The diffractive lenses had an outer radius approaching 9 mm with an inner radius of around 4 mm. The use of circularly polarized light through a second reference beam lens proved to be instrumental in the formation of deep and regular gratings, probably due to the polarization dependency of the formation of gratings in the azobenzene material. Changes to the laser angle of incidence on the sample allowed the formation of multi-focal linear diffractive lenses, while multiple exposures of different geometries on the same sample resulted in custom multi-focal diffractive lenses, although with lower measured diffraction efficiencies. Despite not being as efficient as other fully circular FZPs, this holographic interference lithography method allows for the rapid and cost-effective production of custom diffractive optical elements using off-the-shelf optical components in a single step process without the need for an optical mask. The

speed and ease of this manufacturing method allows from the rapid prototyping and experimental optimization of new technology in research fields such as miniaturization of optics, plasmonics, sensing, communication, and solar energy.

References

[76] O'Shea, D. C., Suleski, T. J., Kathman, A. D. and Prather, D. W., [Diffractive Optics: Design, Fabrication, and Test], SPIE press (2004).

[77] Duval, D., González-Guerrero, A. B., Dante, S., Osmond, J., Monge, R., Fernández, L. J., Zinoviev, K. E., Domínguez, C. and Lechuga, L. M. , "Nanophotonic lab-on-a-chip platforms including novel bimodal interferometers, microfluidics and grating couplers," Lab on a Chip 12(11), 1987-1994 (2012).

[78] Chen, Y., Li, Z., Zhang, Z., Psaltis, D. and Scherer, A. , "Nanoimprinted circular grating distributed feedback dye laser," Appl.Phys.Lett. 91(5), 051109 (2007).

[79] Prather, D. W., Venkataraman, S., Lecompte, M., Kiamilev, F., Mait, J. N. and Simonis, G. J. , "Optoelectronic multichip module integration for chip level optical interconnects," IEEE Photonics Technology Letters 13(10), 1112-1114 (2001).

[80] Banerji, S., Meem, M., Majumder, A., Guevara, F. V., Sensale-Rodriguez, B. and Menon, R. , "Ultra-thin near infrared camera enabled by a flat multi-level diffractive lens," Opt.Lett. 44(22), 5450-5452 (2019).

[81] Vorndran, S. D., Chrysler, B., Wheelwright, B., Angel, R., Holman, Z. and Kostuk, R. , "Off-axis holographic lens spectrum-splitting photovoltaic system for direct and diffuse solar energy conversion," Appl.Opt. 55(27), 7522-7529 (2016).

[82] Dharmavarapu, R., Vijayakumar, A. and Bhattacharya, S. , "Design and fabrication of holographic optical elements for the generation of tilted and accelerating Airy beams," Asian J.Phys. 24(10), 1363-1372 (2015).

[83] Gates, B. D., Xu, Q., Stewart, M., Ryan, D., Willson, C. G. and Whitesides, G. M. , "New approaches to nanofabrication: molding, printing, and other techniques," Chem.Rev. 105(4), 1171-1196 (2005).

[84] Rose, H. W. , "Holographic lens systems," (1973).

[85] Collier, R., [Optical Holography], Elsevier (2013).

[86] Fresnel, A. , "Calcul de I'intensite de la lumiere au centre de l'ombre d'un ecran et d'une ouverture circulaires eclairepar un point radieux," SPIE MILESTONE SERIES MS 128, 3-10 (1996).

[87] Dobson, S. L., Sun, P. and Fainman, Y. , "Diffractive lenses for chromatic confocal imaging," Appl.Opt. 36(20), 4744-4748 (1997).

[88] Koechlin, L., Yadallee, M., Raksasataya, T. and Berdeu, A. , "New progress on the Fresnel imager for UV space astronomy," Astrophysics and Space Science 354(1), 147-153 (2014).

[89] Anand, V., Katkus, T. and Juodkazis, S. , "Randomly multiplexed diffractive lens and axicon for spatial and spectral imaging," Micromachines 11(4), 437 (2020).

[90] Rochon, P., Batalla, E. and Natansohn, A. , "Optically induced surface gratings on azoaromatic polymer films," Appl.Phys.Lett. 66(2), 136-138 (1995).

[91] Priimagi, A. and Shevchenko, A. , "Azopolymer-based micro-and nanopatterning for photonic applications," Journal of polymer science Part B: Polymer physics 52(3), 163-182 (2014).

[92] Oscurato, S. L., Salvatore, M., Maddalena, P. and Ambrosio, A. , "From nanoscopic to macroscopic photo-driven motion in azobenzene-containing materials," Nanophotonics 7(8), 1387-1422 (2018).

[93] Leibold, J. and Sabat, R. G. , "Laser-induced controllable chirped-pitch circular surface-relief diffraction gratings on AZO glass," Photonics Research 3(4), 158-163 (2015).

[94] Sabat, R. G. , "Superimposed surface-relief diffraction grating holographic lenses on azo-polymer films," Optics Express 21(7), 8711-8723 (2013).

[95] Martinez-Ponce, G., Petrova, T., Tomova, N., Dragostinova, V., Todorov, T. and Nikolova, L. , "Bifocal-polarization holographic lens," Opt.Lett. 29(9), 1001-1003 (2004).

[96] Leibold, J. and Sabat, R. G. , "Fabrication of micrometer-scale surface relief gratings in azobenzene molecular glass films using a modified Lloyd's mirror interferometer," Optical Materials 96, 109315 (2019).

[97] Kirby, R., Sabat, R. G., Nunzi, J. and Lebel, O. , "Disperse and disordered: a mexylaminotriazine-substituted azobenzene derivative with superior glass and surface relief grating formation," Journal of Materials Chemistry C 2(5), 841-847 (2014).

[98] Diak, E., Mazloumi, M. and Sabat, R. G. , "Tunable narrowband plasmonic light emission from metallic crossed surface relief gratings," Optics Express 28(26), 39629-39639 (2020).

[99] Fleming, M. B. and Hutley, M. , "Blazed diffractive optics," Appl.Opt. 36(20), 4635-4643 (1997).

[100] Collados, M. V., Chemisana, D. and Atencia, J. , "Holographic solar energy systems: The role of optical elements," Renewable and Sustainable Energy Reviews 59, 130-140 (2016).

[101] Viswanathan, N., Kim, D. and Tripathy, S. , "Surface relief structures on azo polymer films," Journal of Materials Chemistry 9(9), 1941-1955 (1999).

[102] Golub, M. A. , "Laser beam splitting by diffractive optics," Opt.Photonics News 15(2), 36-41 (2004).

[103] Eppig, T., Scholz, K. and Langenbucher, A. , "Assessing the optical performance of multifocal (diffractive) intraocular lenses," Ophthalmic and Physiological Optics 28(5), 467-474 (2008).

CHAPTER 5: THESIS CONCLUSION

This thesis presents 3 published research paper in support of the research goals of advancing interference lithography in DR-1 azoglass and applications in optical sensing. The first goal was to test the upper limits of the pitch in SRGs being inscribed on thin films of DR-1 azoglass using interference lithography. This experiment may be considered a success in that measured pitches of 20 μm were published with measured pitches of 24 μm discovered in follow-on experiments. An unexpected result was the superposition of multiple reflection modes that were inscribed in the DR-1 azoglass film. This allowed for the production of more complicated patterns including beat interference patterns, in a single-step process. The successful results from this first research paper were used as starting point for the second research goal. The second research goal was to measure interference patterns from IL directly on a CMOS imaging sensor. The experiment was originally designed to detect the beat interference pattern from two different reflection modes between the sensor and mirror in the modified Lloyd's mirror interferometer. However, the test results demonstrated interference beat patterns that were caused by the spatial heterodyning of the projected interference pattern with the periodic spacing of the sensor's pixels. This beat interference pattern allows for precise angle measurements better than 8.9 arc seconds in relation to the reference beam using only a small mirror and a very inexpensive sensor component. The third research goal was the direct nanofabrication of diffractive optical devices in DR-1 azoglass using inline holography techniques. This experiment may also be considered a success in that annular FZPs were produced and shown to be able to focus light. This manufacturing technique also proved to be quite flexible as shown by the production of asymmetric linear focal devices and superimposed diffractive lenses. This method could also be used to produce DOEs using other small refractive optics such as axicons. A fourth experiment was attempted using a moving mirror controlled by a piezo electric actuator or a rotating stepper stage. The goal of this experiment was to produce new grating profiles that were not possible with stationary IL techniques. It was also thought that macro scale movement of the DR-1 azoglass material might be possible under the right conditions in order to further the development of DR-1 azoglass actuators. A large amount of effort was put into experimental trials involving the two different set-ups. Unfortunately, the size of the parameter space and the sensitivity of the experiment made it difficult to achieve predictable results. At the same time, another research group published results from a similar moving mirror experiment which reduced the novelty of the idea. As a result of time constraints

and the decrease in novelty, this experiment was put on hold. It may be possible to achieve the desired results in the future with improvements to the precision of the experimental mirror control system.

These research areas are all related to each other by the fact that they rely on interference patterns created from beams of coherent light. Possible applications include the production of miniaturized biosensors, imaging systems, plasmonic devices, and optimized solar cells. These novel IL techniques allow for the rapid manufacturing of a variety of useful surface patterns without the requirement of a photomask. The ease and speed of this fabrication process provides a large advantage for research in the field of optics where diffraction gratings are optimized and tested with different surface patterns. The parameters of the grating can be easily changed based on the geometry of the interfering light and exposure time, and each grating can be manufactured in times scales on the order of minutes. The experimental set-ups use off-the-shelf components that are readily available in most optics labs. This decreases the cost and allows for greater access to diffractions gratings that are customized to specific research application. The development of new IL techniques and sensing methods will only continue to increase the ease and versatility of this nanoscale manufacturing process.

Appendix A: Papers published from research

Leibold, James, and Ribal Georges Sabat. "Fabrication of micrometer-scale surface relief gratings in azobenzene molecular glass films using a modified Lloyd's mirror interferometer." *Optical Materials* 96 (2019): 109315.

Leibold, James, and Ribal Georges Sabat. "Dual-axis optical spatial heterodyning angle measurements using CMOS sensor color crosstalk." Sensors and Actuators A: Physical 303 (2020): 111862.

Leibold, James, and Ribal Georges Sabat. “Inline holographic inscription of diffractive lenses in azobenzene molecular glass thin films.” Applied Optics Vol. 60 No. 10 (2021): 051109.